The Pennsylvania State University

The Graduate School

Aerospace Engineering Department

ANALYSIS OF DUCTED FAN FLOWS USING AN IMMERSED BOUNDARY METHOD

A Thesis in

Aerospace Engineering

by

Kateryna Karachun

Submitted in Partial Fulfillment
of the Requirements
for the Degree of

Master of Science

August 2008

The thesis of Kateryna Karachun was reviewed and approved* by the following:

Philip J. Morris
Boeing/A.D. Welliver Professor of Aerospace Engineering
Thesis Advisor

Kenneth S. Brentner
Professor of Aerospace Engineering

John B. Fahnline
Applied Research Lab

George A. Lesieutre
Head of the Department of Aerospace Engineering

*Signatures are on file in the Graduate School

Abstract

The Cartesian immersed boundary code "CARIBOU" has been used for several validation cases and to compute the flow field for a rotating blade and a ducted fan. First, the code is used to calculate the flow solution for a rotating cylinder in a quiescent medium. Second, the code is used to model the Stokes's second problem of a wall oscillating in its plane. Third, the relationship between the viscous and inviscid versions of the CARIBOU code is established by initiating flow over NACA0009 airfoil. If the grid spacing in the inviscid code is such that, $\Delta y = \mathrm{Re}^{(-3/4)}$, then the viscous code with that particular Reynolds number yields the same flow solution as the inviscid code. After these tests, the 3D inviscid version of the code is used for the remainder of the project work. The last validation of CARIBOU confirms that if all parameters are initiated identically, stationary and moving coordinate systems in CARIBOU calculate identical flow solutions. Hence, modeling of the flow for a rotating blade used only moving grids in order to keep the number of points as small as possible and to reduce the computational time. A comparison between a rotating blade far from the point of rotation with a translating blade was satisfactory. For both cases, the lift force distribution was similar.

Although the inviscid code with a moving grid was used for the rotating blade study, the full analysis of the flow was not carried out due to the unreasonably long time required by the computations. Nevertheless, collected data show that the lift force, for the early stages of flow development, oscillates about the average lift curve, which is also predicted theoretically.

For the ducted fan study the fan is represented by a classical pressure jump. Three duct geometries are analyzed with the 2D serial version of the CARIBOU code. The flow computations, for all three ducts, show wake expansion at the exit of the duct, which agrees well with theory. However, the flow analyses show that duct geometry influences the wake development downstream.

Table of Contents

List of Figures

Acknowledgements

I would like to thank my advisor, Dr. Philip J. Morris, for giving me an opportunity to work on this project and for his invaluable guidance throughout my academic program. Also, I would like to thank Dr. Kenneth Brentner, and Dr. John Fahnline, for their thoughtful insight and persistent help with my research work.

I would like to thank the Applied Research Laboratory for financial support throughout my stay at Penn State University.

Additionally, I would like to thank Jogesh Chopra for helping me learn the CARIBOU code and Kirk Heller for prompt help with cocoa3 and other technical difficulties that have come up during research.

Lastly, I would like to thank my family and Adrian P. for their persistent support and encouragement.

1

Introduction

Ducted fans have become an appealing alternative as a propulsion system for vertical take-off aircraft, such as the BELL X-22A, helicopters and especially unmanned aerial vehicles (UAVs). For example, UAVs including Sikorsky's Cypher, Aurora's GoldenEye, iSTAR and many others successfully integrated ducted fans as propulsive devices. The UAVs are compact and light, hence they are efficient for vertical take-off and landing.[1]

Ducted fans have numerous advantages over conventional open rotors. First, ducted fans consume about 30% less power than an open rotor for the same net thrust[2]. Consequently, if the disk area of a ducted fan is reduced by half that of a conventional rotor, it will produce the same thrust and consume the same power[2]. Hence, a vehicle designed with ducted fan propulsion can be more compact and better suited for operating in confined spaces[3]. Second, the shroud around the rotor provides safety. It protects blade tips from surrounding hazards and it protects people from the rotating blades. Third, vanes can be attached to the top or bottom surface of a ducted fan for primary flight control, thereby creating redundancy for the control system or simply reducing its complexity[3]. Lastly, the rotor shroud helps to shield the noise produced by the embedded rotating fan[3].

One of the first systematic studies conducted on ducted fans was by Kruger[4] in 1949. This is described in his seminal paper entitled "On Wind Tunnel Tests and

Computations Concerning the Problem of Shrouded Propellers". In the 1960's, NASA, at the Ames Research Center, conducted several advanced wind tunnel tests on shrouded propellers.[5-6] As a result, extensive data was collected on thrust, drag and efficiency of scale models and prototypes. Also, in the 1970's, experiments conducted in the United Kingdom validated the claim that the ducted propeller is an effective propulsion system.[1] Recent research studies include NASA experiments on a ducted fan for a personal transport rotorcraft and application as an antitorque device, as in the fenestron or FANTAIL.[7] Additionally, Martin et al. [7] have performed experiments for a new class of small UAVs, also known as micro UAVs.

Although, ducted fan propulsion is used in various applications and has been extensively studied, there is still a lot of unknown information about its capabilities and aerodynamics, especially in maneuvers. Therefore, the objective of this thesis is to model a ducted fan using an in-house Cartesian immersed boundary code "CARIBOU" to help provide a better understanding of the capabilities of ducted fans.

Computational fluid dynamics (CFD) codes are used extensively in modeling ducted fans. One approach is to utilize the momentum method for the computations and represent the ducted fan system rotor inside the shroud by an actuator disk model[8]. This type of model can be used to make approximate predictions of thrust and power. However, it cannot be used to model nonuniform flow or interactions between the fan and the duct. To compensate for these shortcomings, Ahn et al. [8] describe a method where a model fan is represented as an axisymmetric actuator disk with non-uniform radial strength distribution which also includes the blade tip loss. In this case, the actuator disk provides discontinuities in stagnation enthalpy and stagnation density.[8] This model is solved on a body-fitted grid by an Euler solution method.

Another CFD code designed for determining the overall performance of ducted fans implicitly introduces the effect of rotating blades in the form of a force into the governing equations.[1] Chang et al. [1] state that since the momentum equations govern the balance of the rate of change of momentum and the external forces experienced by the fluid element, the force created by the rotating blade can be included as a momentum source at the cells occupied by the blade at one particular moment. Calculations have been performed on an axisymmetric Cartesian grid with a curve adaptive option and the

discretized equations are solved using a finite-volume approach called SIMPLER. This uses an iterative procedure to solve for the primitive variables.[1]

More detailed three-dimensional analysis of a shrouded helicopter tail rotor is described by Lee et al.[9] in their study paper, "Aerodynamic Performance Analysis of a Helicopter Shrouded Tail Rotor using an Unstructured Mesh Flow Solver". In this study, the rotor is represented by a three-dimensional point sink, with strength equivalent to the mass flow rate through the far-field boundary which is obtained from momentum theory.[9] The calculations are performed using an unstructured mesh Euler flow solver and are made for a single blade of the rotor by imposing a periodic boundary condition between blades.

The CFD code, CARIBOU (Cartesian Immersed Boundary), used in present research, performs calculations on a structured Cartesian grid with an immersed boundary approach. This methodology allows for the grid to be generated only once for either stationary or moving bodies. Hence, the rotating fan with or without a duct, can be modeled using this method without regenerating the grid at every time step. The uniform Cartesian grid does not always provide the user with a well defined geometry. In this case, a large number of grid points in the vicinity of the body are necessary for an exact body representation. Sometimes, a large number of grid points are needed to correctly model flow within the boundary layers. However, as the number of grid points increases, so does the computational time. In order to overcome this effect, a stretched Cartesian grid can be implemented. Stretching of the grid allows the user to use more grid points near the body boundary and fewer points elsewhere in the domain.

In CARIBOU, the immersed boundary method represents the impact of the body on the surrounding medium by the introduction of a fictitious force. This approach is known as the Brinkman penalization method.[10] The compressible and incompressible Navier-Stokes equations are implemented in the computational method. The numerical implementation of the code uses a 4^{th} order Runge-Kutta method for time marching and a Weighted Essentially Non-Oscillatory (WENO) scheme to eliminate any spurious numerical oscillations. A moving coordinate system is also used in CARIBOU to simplify the problem set-up and reduce the computational time. In the following chapter, a more complete description of CARIBOU is given.

There are several versions of the CARIBOU code. The 2D serial version is used for simple and quick calculations and the 2D and 3D parallel versions are used for more complex problems. The validations described in Chapter 3 are performed using one of the versions of the code. The rotating cylinder and oscillating wall cases are simulated using the 2D viscous, serial code. The translating blade case is simulated using the 3D viscous and inviscid parallel codes. Comparison between moving and stationary grids is also accomplished by translating the blade in the 3D inviscid parallel code. Also, the same version of the code is used for both rotating blade cases and for generating a pressure jump in a duct.

The majority of the work performed for this thesis involves the simulation of flows over several geometries. Therefore, original contributions to the CARIBOU code consist of the development of different types of boundary conditions and initial conditions based on the initial parameters of a given problem. Also, two 3D duct geometries have been developed and the flows in them have been simulated.

In the next chapter the immersed boundary method and the CARIBOU code are described. The following chapter describes the cases that were used to validate and study CARIBOU's capabilities. Chapter 4 contains the description and analyses of the two cases of the rotating blade. Similarly, Chapter 5 contains the description and analyses of the simulation of the pressure jump for three duct geometries. Finally, some concluding remarks and suggestions for future work are given in Chapter 6.

2

The CARIBOU Code

Traditionally, the simulation of the flow past a solid body would employ either structured or unstructured, body fitted grids. The grids are generated by first covering the surface of the body and then the volume occupied by the fluid.[11] These grids are known as body-fitted grids, because they conform to the geometry of the body. When the body is rigid, the computations are carried out with relative ease. However, when the body is flexible, the grid needs to be regenerated every time step or distorted around the moving surfaces.[12] These cumbersome operations increase computational cost, complicate the process, and reduce the accuracy and robustness of solution.[11] Therefore, another computational method has been developed to eliminate the grid generation complexity. This method is known as the "Immersed Boundary Method". The idea of this method is that numerical calculations can be performed on structured Cartesian grids regardless of the complexity of the geometry or motion of the body.[12] This method was first referenced in Charles Peskin's work in 1972, where he simulated blood flow through a pumping heart on a structured Cartesian grid.[11,13] The basic idea of the Immersed Boundary Method has been implemented in many flow simulation methods; one of which – CARIBOU – is the program used in the present thesis work. This chapter gives a brief description of the ideas implemented in the CARIBOU code.

Governing Equations

The CARIBOU code uses the three-dimensional Navier-Stokes equations. The governing equations are non-dimensionalized with respect to the following quantities: length, L^*, velocity, a^*, density, ρ^*, temperature, T^*, viscosity, μ^*, pressure, $\rho^*(a^*)^2$, viscous stress, $\mu^* a^* / L^*$, where L^* is one unit length (when an airfoil is used, L^* is the chord length of that airfoil), a^* is the speed of sound in all of the cases. Variables with an asterisk are dimensional quantities. Then, the non-dimensional viscous Navier-Stokes equations in Cartesian tensor form can be written as:

$$\frac{\partial \rho}{\partial t} + \frac{\partial}{\partial x_i}(\rho u_i) = 0$$

$$\frac{\partial}{\partial t}(\rho u_i) + \frac{\partial}{\partial x_j}(\rho u_i u_j + p\delta_{ij}) = \frac{\partial \tau_{ij}}{\partial x_j}$$

$$\frac{\partial}{\partial t}(\rho e_t) + \frac{\partial}{\partial x_j}(\rho u_j e_t + p u_j) = \frac{\partial}{\partial x_j}(u_j \tau_{ij} - q_j)$$

where, e_t is the total energy and is defined as:

$$e_t = \frac{T}{\gamma(\gamma - 1)} + \frac{1}{2}(u_i u_i)$$

where, $\gamma = c_p / c_v = 1.4$.

Pressure in CARIBOU is defined by the ideal gas law, $p = \frac{\rho T}{\gamma}$, so that

$$p = (\gamma - 1)\rho\left[e_t - \frac{1}{2}(u_i u_i)\right]$$

The fluid is Newtonian, hence the linear stress strain relationship is used. It is given by,

$$\tau_{ij} = \frac{M}{\mathrm{Re}}\left[\mu\left(\frac{\partial u_i}{\partial x_j} + \frac{\partial u_j}{\partial x_i}\right) + \lambda \frac{\partial u_k}{\partial x_k}\delta_{ij}\right]$$

where, M is the Mach number, Re is the Reynolds number, μ is the dynamic coefficient of viscosity and λ is the bulk coefficient of viscosity. The heat transfer term in the energy equation is formed by Fourier's law of heat conduction,

$$q_j = -\frac{1}{\gamma - 1}\frac{M}{\mathrm{Re}}\frac{\mu}{\mathrm{Pr}_L}\left(\frac{\partial T}{\partial x_j}\right)$$

where Pr_L is the laminar Prandtl number.

Immersed Boundary method in CARIBOU

When the cross section of the body is embedded into a Cartesian grid, its realistic boundary cuts through the grid and therefore the points that lie outside the boundary and inside of the body can be determined. In CARIBOU, the user assigns a value of one to points inside the body and a value of zero to points outside. Using these weights as multiplicative factors then allows forces to be applied to only the points inside the boundary. As can be observed in Figure 1, the computational boundary (green line) is step-like. Therefore, it is important to note that the grid spacing (Δy and Δx) around the surface of the body should be set as small as possible, so that the difference between the computational and physical boundaries is minimal.

The computational boundary is defined as the Immersed Boundary in the code. The governing equations then can be discretized using finite difference or other techniques, without resorting to coordinate transformation or complex discretization operators.[11]

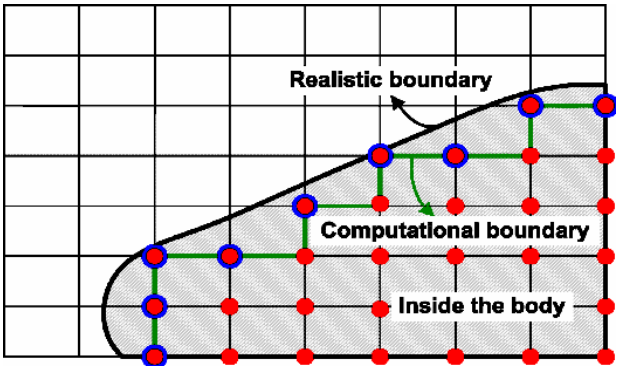

Figure 1 Sketch of the realistic and computational boundaries of an airfoil section[12]

Equations of motion, Brinkman's Penalization

CARIBOU uses the Brinkman's Penalization Method.[12] This method represents the effect of the body by a fictitious body force in the momentum equations. As a result, the compressible governing equations of motion take the following form:

$$\frac{\partial \rho}{\partial t} + \frac{\partial}{\partial x_i}(\rho u_i) = 0$$

$$\frac{\partial}{\partial t}(\rho u_i) + \frac{\partial}{\partial x_j}(\rho u_i u_j + p\delta_{ij}) = \frac{\partial \tau_{ij}}{\partial x_j} + f_i$$

$$\frac{\partial}{\partial t}(\rho e_t) + \frac{\partial}{\partial x_j}(\rho u_j e_t + p u_j) = \frac{\partial}{\partial x_j}(u_j \tau_{ij} - q_j)$$

The f_i term is the body force that sets the flow to zero or to a given velocity within the body.[12] This method was modified by Mohd-Yusof[14], who applied the penalization force to the discretized form of the momentum equations.[12] Thus, the momentum equation takes the following form:

$$\frac{\rho u_i^{n+1} - \rho u_i^{n}}{\Delta t} = RHS_i + f_i$$

where, RHS_i contains all the convective and viscous terms and the pressure gradient.[12] This equation can then be solved for the fictitious force:

$$f_i = \begin{cases} 0 & , outside\,the\,body \\ -RHS_i + \rho(v_{bi}^{n+1} - u_i^{n})/\Delta t & , inside\ the\,body \end{cases}$$

where, the v_{bi}^{n+1} term is the velocity of the body at the $(n+1)th$ time step. Therefore, it can be seen that, at the end of the time step, $u_i^{n+1} = v_{bi}^{n+1}$ inside the body.[12]

Turbulence Model in CARIBOU

Menter's shear stress transport $k-\omega$ turbulence model (SST)[15] is used in CARIBOU to compute turbulent flows. This model is represented by the following equations:

$$\frac{\partial}{\partial t}(\rho k) + \frac{\partial}{\partial x_j}(\rho u_j k) = P_k - \beta^* \rho \omega k + \frac{\partial}{\partial x_j}\left[(\mu + \sigma_k \mu_t)\frac{\partial k}{\partial x_j}\right]$$

$$\frac{\partial}{\partial t}(\rho \omega) + \frac{\partial}{\partial x_j}(\rho u_j \omega) = \gamma P_\omega - \beta^* \rho \omega^2 + \frac{\partial}{\partial x_j}\left[(\mu + \sigma_k \mu_t)\frac{\partial \omega}{\partial x_j}\right] + 2(1-F_1)\sigma_{\omega 2}\frac{1}{\omega}\frac{\partial k}{\partial x_j}\frac{\partial \omega}{\partial x_j}$$

All of the parameters in the equations and the model coefficients are defined in Menter's paper.[15] Inside the body, turbulence is neither generated nor dissipated.[12] Therefore, the kinetic energy, *k*, on the surface and inside the body is set to zero. The specific dissipation rate, ω, is set to the free-stream value. Hence,

$$k_w = 0 \quad \text{and} \quad \omega_w = \frac{20\nu}{\beta(\Delta y_1)^2}$$

where, $\beta = 3/20$ and Δy_1 is the distance from the wall to the nearest external grid point.

In the SST model, the specific dissipation rate at the wall, the eddy viscosity, and a blending function of the original and transformed models depend on the distance from a point in the flow field to the wall. In CARIBOU, this distance is approximated as the distance from the wall to the nearest node point inside of the body. Cho et al. [12] state that such a definition prevents the distance becoming extremely small as the body surface moves close to a fixed grid point. The grid points on the boundary where the dissipation rate is specified use distance to the nearest neighboring point outside of the body.[12]

Numerical Implementation:

Weighted Essentially Non-Oscillatory (WENO) scheme

The compressible Navier-Stokes equations and the two turbulence equations in CARIBOU are discretized spatially using a 5th order Weighted Essentially Non-Oscillatory (WENO) scheme. The WENO scheme helps eliminate any discontinuities that may occur in the flow variables or their derivatives. This is especially helpful in the immersed boundary method because the fictitious body boundary represents a discontinuity in the flow variables. Hence, it is important to minimize oscillations that can occur there. Cho et al. [12] describe the WENO scheme using the one dimensional equation,

$$\frac{\partial u}{\partial t} + \frac{\partial q(u)}{\partial x} = 0$$

where the flux q can be discretized by the following finite difference equation,

$$\left.\frac{\partial q}{\partial x}\right|_{x=x_i} = \frac{\hat{q}_{i+1/2} - \hat{q}_{i-1/2}}{\Delta x}$$

Then using the 5th order WENO scheme, the flux $\tilde{q}_{i+1/2}$ (for example) can be defined by the following three 3rd order fluxes,[12]

$$\hat{q}^{(1)}_{i+1/2} = \frac{1}{3}q_{i-2} - \frac{7}{6}q_{i-1} + \frac{11}{6}q_i$$

$$\hat{q}^{(2)}_{i+1/2} = -\frac{1}{6}q_{i-1} + \frac{5}{6}q_i + \frac{1}{3}q_{i+1}$$

$$\hat{q}^{(3)}_{i+1/2} = \frac{1}{3}q_i + \frac{5}{6}q_{i+1} - \frac{1}{6}q_{i+2}$$

So that,

$$\hat{q}_{i+1/2} = \omega_1\hat{q}^{(1)}_{i+1/2} + \omega_2\hat{q}^{(2)}_{i+1/2} + \omega_3\hat{q}^{(3)}_{i+1/2}$$

The ω_j are nonlinear weights that can be calculated using the equations:

$$\omega_j = \frac{\alpha_j}{\sum_{k=1}^{3}\alpha_k}, \quad \alpha_k = \frac{d_k}{(\varepsilon + \beta_k)^2}$$

where, d_k are linear weights and are equal to 1/10, 3/5, and 3/10 respectively.[12] To prevent a zero value in the denominator, the constant ε is set to 1×10^{-6} and added to the smoothness indicators, β_k. The smoothness indicators calculate the smallest weight for the stencils in regions where fluxes oscillate rapidly.[12] The indicators are represented by the following equations,

$$\beta_1 = \frac{13}{12}(q_{i-2} - 2q_{i-1} + q_i)^2 + \frac{1}{4}(q_{i-2} - 4q_{i-1} + 3q_i)^2$$
$$\beta_2 = \frac{13}{12}(q_{i-1} - 2q_i + q_{i+1})^2 + \frac{1}{4}(q_{i-1} - q_{i+1})^2$$
$$\beta_3 = \frac{13}{12}(q_i - 2q_{i+1} + q_{i+2})^2 + \frac{1}{4}(3q_i - 4q_{i+1} + q_{i+2})^2$$

A more detailed description of WENO schemes in general is given by Shu.[16]

Runge-Kutta Method

Time advancement in CARIBOU is achieved using a fourth order Runge-Kutta scheme[17] for both the steady and unsteady flows. The explicit scheme for temporal discretization for one dimension is defined by:

$$\frac{Q'-Q^n}{\Delta t} = k_1 \frac{\partial E^n}{\partial x}$$
$$\frac{Q''-Q'}{\Delta t} = k_2 \frac{\partial E'}{\partial x}$$
$$\frac{Q'''-Q''}{\Delta t} = k_3 \frac{\partial E''}{\partial x}$$
$$\frac{Q^{n+1}-Q'''}{\Delta t} = k_4 \frac{\partial E}{\partial x}$$

where,

$$Q = \begin{Bmatrix} \rho \\ \rho u \\ \rho v \\ \rho w \\ \rho e_t \end{Bmatrix} \qquad E = \begin{Bmatrix} \rho u \\ \rho u^2 + p - \tau_{xx} \\ \rho uv - \tau_{xy} \\ \rho uw - \tau_{xz} \\ (\rho e_t + p)u - u\tau_{xx} - v\tau_{xy} - w\tau_{xz} + q_x \end{Bmatrix}$$

For the other two dimensions, the right hand side equals the Runge-Kutta coeffieint, k_i, multiplied by $\frac{\partial F}{\partial y}$ or $\frac{\partial G}{\partial z}$, where,

$$F = \begin{Bmatrix} \rho v \\ \rho vu - \tau_{yx} \\ \rho v^2 + p - \tau_{yy} \\ \rho vw - \tau_{yz} \\ (\rho e_t + p)v - u\tau_{xy} - v\tau_{yy} - w\tau_{zy} + q_y \end{Bmatrix} \quad G = \begin{Bmatrix} \rho w \\ \rho wu - \tau_{zx} \\ \rho wv - \tau_{zy} \\ \rho w^2 + p - \tau_{zz} \\ (\rho e_t + p)w - u\tau_{xz} - v\tau_{yz} - w\tau_{zz} + q_z \end{Bmatrix}$$

The weights in the scheme, k_1, k_2, k_3, k_4 are 1/4, 1/3, 1/2, 1 for unsteady time accurate simulations, and 3/8, 1/2, 1, 1 for accelerated convergence of the solution in a steady state calculation.[18]

Moving Coordinate System

In a simulation where the body is moving, a large number of grid points and an extended domain is necessary. A fine grid is required around the moving boundary at every time step and the computational domain must include the path of the moving body. These requirements can overwhelm the computer system. Therefore, it is more efficient to use a moving coordinate system (MCS).[19] In a MCS, the grid moves with the body and all compressible governing equations of motion and the turbulence $k-\omega$ equations are calculated with respect to the relative velocity and the free stream velocity.

$$\frac{\partial \rho}{\partial t} + \frac{\partial}{\partial x_i}(\rho u_i^r) = 0$$

$$\frac{\partial}{\partial t}(\rho u_i) + \frac{\partial}{\partial x_j}(\rho u_i u_j^r + p\delta_{ij}) = \frac{\partial \tau_{ij}}{\partial x_j} + f_i$$

$$\frac{\partial}{\partial t}(\rho e_t) + \frac{\partial}{\partial x_j}(\rho u_j^r e_t + p u_j^r) = \frac{\partial}{\partial x_j}(u_j^r \tau_{ij} - q_j)$$

$$\frac{\partial}{\partial t}(\rho k) + \frac{\partial}{\partial x_j}(\rho u_j^r k) = P_k - \beta^* \rho \omega k + \frac{\partial}{\partial x_j}\left[(\mu + \sigma_k \mu_t)\frac{\partial k}{\partial x_j}\right]$$

$$\frac{\partial}{\partial t}(\rho \omega) + \frac{\partial}{\partial x_j}(\rho u_j^r \omega) = \gamma P_\omega - \beta^* \rho \omega^2 + \frac{\partial}{\partial x_j}\left[(\mu + \sigma_k \mu_t)\frac{\partial \omega}{\partial x_j}\right] + 2(1 - F_1)\sigma_{\omega 2}\frac{1}{\omega}\frac{\partial k}{\partial x_j}\frac{\partial \omega}{\partial x_j}$$

where, the relative velocity, u_i^r is defined by the difference between free stream velocity and velocity of the grid, $u_i^r = u_i - u_i^g$, where u_i^g is the velocity of the grid.[12]

A brief description of the CARIBOU code and immersed boundary method has been given in this chapter. In the following chapter, cases that assess the CARIBOU code are described in detail.

3

Validation of CARIBOU

Before beginning to work on ducted fan problems, several flow cases were simulated in 2D and 3D to evaluate the CARIBOU code. The first problem is a rotating cylinder. The second one is an oscillating wall, which is validated by comparison with analytical solutions to Stokes's second problem. Then the relationship between the viscous and inviscid codes is demonstrated by simulation of flow around a short translating blade. The advantage of a moving coordinate system is established by translation of an infinitely long blade. It should be noted that all quantities are non-dimensional. Length is non-dimensionalized by one unit length, L^* and velocity by the speed of sound, a^*. As mentioned before, an asterisk indicates that a variable is dimensional.

Rotating Cylinder

In this example, a cylinder is rotating in a quiescent viscous medium. The goal is to simulate the resulting flow field. The cylinder is solid inside and appears as a circle in the *xy*-plane. The body is located in the center of the domain at $x = y = 0$, with a radius of 0.5 units. The grid is uniform from -0.5 to 0.5 and stretched from -0.5 to -10 and 0.5 to 10 in both directions. The grid spacing in the center region is $\Delta x_{\min} = \Delta y_{\min} = 0.05$. The total number of points used in each direction is 100, with 20x20 in the uniform portion of the grid, and the rest in the stretched portion of the grid.

The rotation of the cylinder is simulated by setting a body velocity, Vb in the x and y directions, to the following:

$$Vb_x = -\omega * r_y$$
$$Vb_y = \omega * r_x$$

where, ω is the non-dimensional angular velocity of the cylinder, which equals -0.5π; r_x, r_y are the components of the radius at a point in the x and y directions respectively. The point of rotation is at the origin which coincides with the center of the cylinder. The Reynolds number, Re, in this case was chosen to be 10^5, based on angular velocity at the cylinder boundary and the radius of the cylinder.

Figure 2 shows how, after some time, the flow is developed around the rotating cylinder. The velocity is high near the surface and slowly decreases outward into the stationary medium. Figure 2 also shows that there is a velocity distribution inside the cylinder, this is not a flow velocity, it is a body velocity which initiates rotation. Velocity components, u and v, are plotted along the x and y axes in Figure 3. This shows how the boundary layer has developed on the surface of the cylinder. Also, it can be observed that flow is axisymmetric.

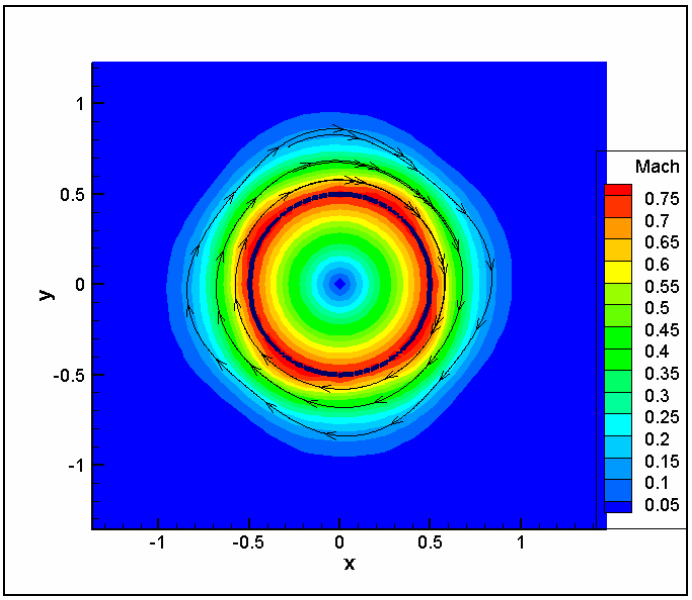

Figure 2 Mach contours inside and around rotating cylinder. Streamtraces show the direction of rotation

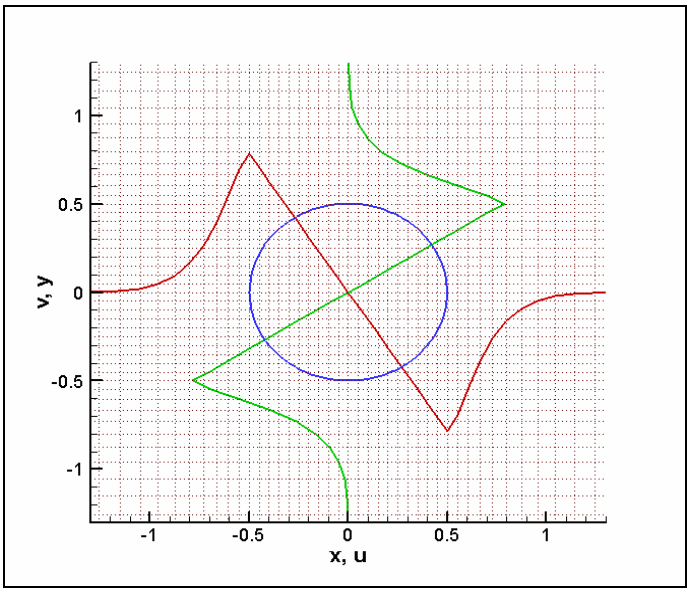

Figure 3 Velocities, u (green line) along y and v (red line) along x

Oscillating Wall

The second example simulated in the 2D CARIBOU code is an oscillating wall. Stokes's second problem is used to set up the simulation and initiate oscillation. The problem describes laminar flow produced by plate oscillating in its plane with velocity, $u = U\sin(\omega t)$, where ω is the angular frequency and U is the maximum velocity of the wall in the x direction.[20] The boundary conditions for this problem, which are also used in CARIBOU, are as follows: for $y = 0$, $u(t) = U\cos(\omega t)$ and for $y = \infty$, $u(t) \to 0$.[20] Assuming the wall is oscillating for a long time, a theoretical solution for the flow is given by the following equation, $u(y,t) = Ue^{-ky}\cos(\omega t - ky)$, where $k = \sqrt{\omega/2\nu}$ and ν is the kinematic viscosity.[20] By non-dimensioning y by k^{-1}, a new variable is defined $\eta = y/k^{-1} = y/\sqrt{\omega/2\nu}$, and therefore, the non-dimensional exact flow equation becomes $f = u/U = e^{-\eta}\cos(\omega t - \eta)$.[20]

The domain used in this example is $-10 \le x, y \le 10$. The grid is stretched in the y direction from -10 to 0 with $\Delta y_{\min} = 0.01$ using only 10 points, and from 0 to 10 with the

same $\Delta y_{\min}$, but using 90 points. Fewer points are used in the portion of the grid where the body is positioned, because that area will not be considered for analysis. In the x direction, the grid is uniform throughout with $\Delta x = 0.2$ for all 100 points.

The oscillating wall is represented by a rectangle that is set from -10 to 0 in the y direction and from -7 to 7 in the x direction. Since the wall oscillates in the x-direction and some space is necessary for it to move, the wall does not extend all the way to the boundaries. However, Stokes's second problem assumes an infinite plate; therefore in CARIBOU, boundaries and grid points between the boundaries and the wall edges for $y \le 0$ are set to boundary velocities defined by Stokes's second problem. That way, an oscillating rectangle appears like an infinite wall. For this example, the non-dimensional angular frequency is set to either 0.5 or 1, and the non-dimensional U is 0.3. Thus, velocities at the boundaries and grid points which do not include the body for $y \le 0$ are set to:

$$u = 0.3\cos(1.0 * t)$$
$$v = 0.0$$

Boundaries in the range $0 \le y \le 10$ are periodic. Oscillation of the wall, as mentioned before, is also defined by Stokes's second problem. Using set quantities, body velocities are:

$$Vb_x = 0.3\sin(1.0 * t)$$
$$Vb_y = 0.0$$

The Reynolds number in this case is equal to 10^3, based on the magnitude of the oscillating wall velocity and $\Delta y_{\min}$.

In Figures 4 and 5, the velocity in the x-direction, u, is plotted as a function of y for the numerical and exact solutions at ω = 1 and 0.5, respectively. The theoretical solution is given as a function of η in the previous equations (see Appendix C for the calculation of the theoretical solution). Both figures show that numerical and theoretical solutions for Stokes's second problem match well.

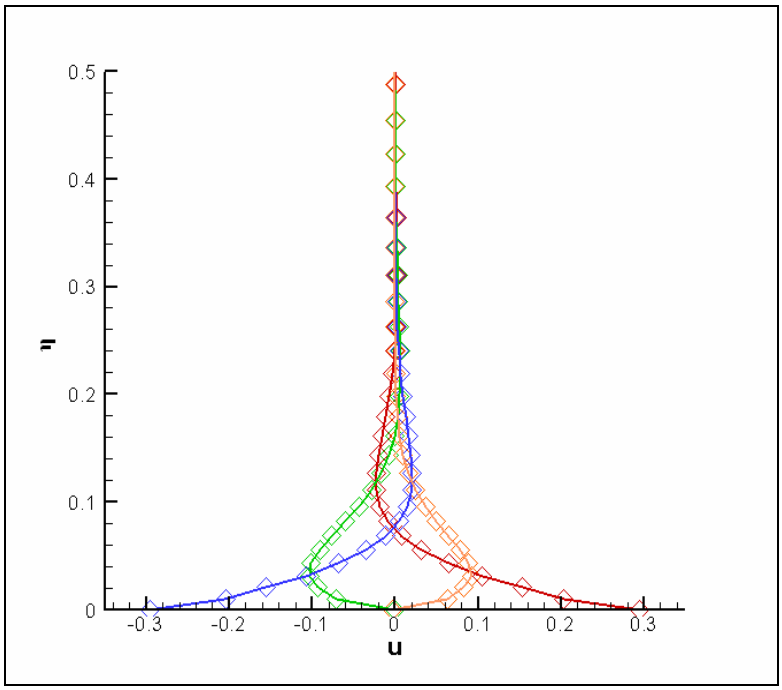

Figure 4 Comparison of numerical (symbols) and exact (solid lines) solutions for oscillating wall, $\omega = 1$

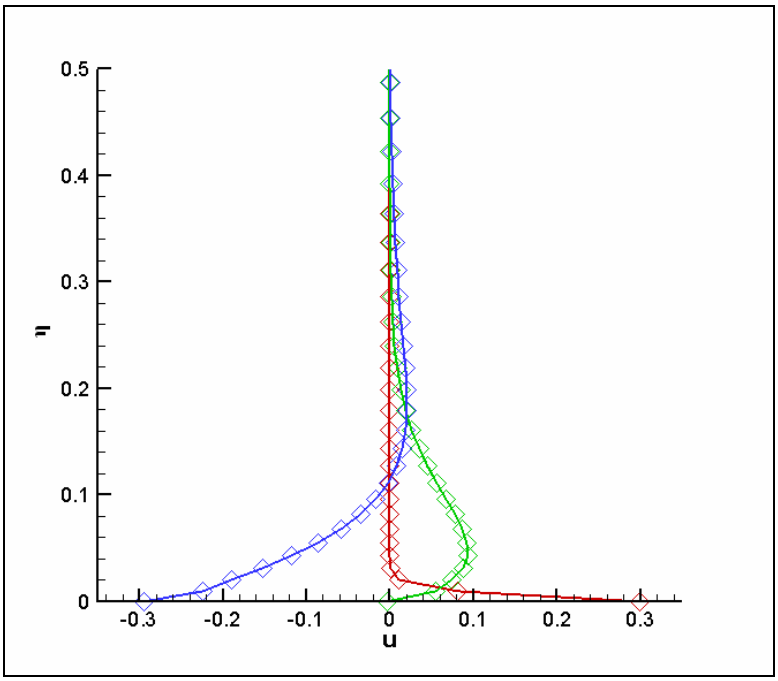

Figure 5 Comparison of numerical (symbols) and exact (solid lines) solutions for oscillating wall, $\omega = 0.5$

Inviscid vs. viscous CARIBOU codes

Simulating problems using the 3D viscous code is challenging because more grid points are required to resolve the flow field and more processors are needed to run the code. Therefore, it is desirable to use the inviscid version of the code, because it runs faster. Viscous and inviscid codes are linked by the Reynolds number and grid resolution in the *y*-direction in the viscous boundary layer (assuming that the *xy* plane is the cross sectional plane and the *y* direction is vertical). For a given Reynolds number, $\Delta y_{\min}$ can be calculated by the following equation: $\Delta y_{\min} = \mathrm{Re}^{(-3/4)}$.[21] When the calculated $\Delta y_{\min}$ is used in inviscid code, the flow solution will resemble that of viscous code with a corresponding Reynolds number. Similarly, the Reynolds number can be calculated for a selected $\Delta y_{\min}$.

To test the accuracy of the inviscid simulation, the viscous and inviscid codes are used to compute flow over a stationary NACA 0009 short blade in a stationary grid with 120x150x41 grid points in the *x*, *y*, and *z* directions, respectively. The domain is set to $-10c \le x, y, z \le 10c$ (c is the chord length of the airfoil). At this grid resolution, the lift and drag coefficients are not expected to converge to the correct values, as discussed by Cho et al.[12] However, the relatively coarse grid allows the 3D viscous code to run on only 12 processors and yields reasonable computation times.

The chord of the airfoil is taken to be 1 and it is set in the middle of the *xy*-plane between $-0.5c \le x \le 0.5c$. The span in the *z* direction is also 1 and it is positioned between $-0.5c \le z \le 0.5c$. The grid is clustered in the vicinity of the blade with $\Delta x_{\min} = 0.01c$, $\Delta y_{\min} = 0.0012c$, $\Delta z_{\min} = 0.1c$. The calculated Reynolds number for a given $\Delta y_{\min}$ is 7841. In both cases the airfoil is aligned with the grid and the flow is generated at an angle of 4 degrees from the *x*-grid lines with a non-dimensional velocity of 0.5.

Figure 6 shows the convergence for the lift coefficient for both viscous and inviscid codes. The predicted results match well. Therefore, it was decided to run future cases only with the inviscid code in order to reduce the time it takes for calculations. Unfortunately, the inviscid code sometimes requires a very small $\Delta y_{\min}$ near the interface between the fluid and structure to reduce unphysical vortices. Consequently more grid

points are used to resolve these flow anomalies and more processors are needed to run calculations. However, even with this negative aspect, the inviscid code is still more computationally efficient than the viscous code.

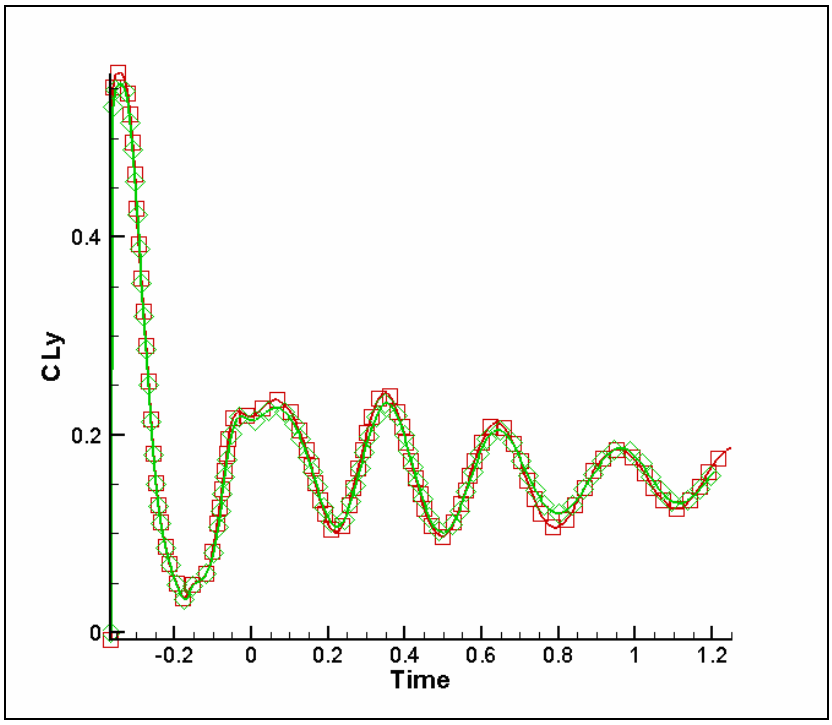

Figure 6 Lift coefficient convergence for viscous (green) and inviscid (red) codes

Moving vs. Stationary Grid

It is preferable to use a moving grid rather than a stationary grid for several reasons. First, when a body is moving, the computational domain does not have to extend throughout the entire path of the body to trace its motion. The domain can be sized specifically to analyze the flow around the body. Consequently, less grid points are necessary. Therefore, the computation time is greatly reduced. Second, there is no need for separate calculations to define the motion of the body as it moves with the moving grid. However, additional calculations are required to initiate the motion of the grid. But they are usually simpler. Third, with a stationary grid, the body definition has to be

recalculated every time step. However, with a moving grid, the body is defined only once.

The comparison between moving and stationary grids is performed, as in the previous example, by simulating flow over a NACA 0009 blade. For both cases, the inviscid 3D CARIBOU code is used. The domain is set to $-20c \le x, y \le 20c$ and $-0.2c \le z \le 0.2c$. The grid dimensions are 330x380x6 in the x, y, and z directions respectively. The grid is clustered in the area where the body is positioned using the following minimum values: $\Delta x_{\min} = 0.001c$, $\Delta y_{\min} = 0.0005c$, $\Delta z_{\min} = 0.1c$. The airfoil is positioned in the grid the same way as in the previous case, the chord of the airfoil is 1 and set in the middle of the xy-plane between $-0.5c \le x \le 0.5c$. However, in this case the body does not have a finite span, and it stretches throughout all the domain in the z-direction. Consequently, the boundaries are set to be periodic in the spanwise direction. Hence the flow solution actually becomes nearly 2D.

For both cases, the airfoil is set in two positions. In the first position, the airfoil is aligned with the grid (Figure 7) and in the second it is set at angle of 4 degrees but the grid is kept in its original horizontal setting (Figure 8). The goal is to study which situation will result in a better agreement between stationary and translating airfoils.

When the airfoil is aligned with the grid, for the stationary airfoil case, a non-dimensional velocity of 0.2 is generated in the x direction at angle of 4 degrees. For the moving case, the grid and airfoil are moving to the left at an angle of 4 degrees with a non-dimensional velocity of 0.2 as well. Correspondingly, when the airfoil is set at an angle with respect to the grid, for the stationary case, a velocity of the same magnitude is generated at an angle of 0 degrees. For the moving case, the grid is set at 0 degrees and both the grid and airfoil are translating to the left with same non-dimensional velocity of 0.2.

The lift and drag coefficients are plotted for comparison for each case in Figures 9 - 12. It can be observed that when the airfoil is aligned with the grid, lift and drag coefficients agree better for stationary and translating airfoils than when the airfoil is at an angle with respect to the grid. When the immersed boundary method is used, a body is represented by the closest grid points to its edges (boundaries). Therefore when an airfoil is aligned with the grid, the body is better represented by the surrounding grid points. In

the case of the airfoil set at an angle, the body boundary lines cut through grid points at a steeper angle and the airfoil surface in the code appears rougher. Flow over a rough surface appears more unstable and the convergence is more oscillatory. Hence, the case which has smoother, well defined airfoil geometry is expected to give better results.

Nevertheless, as Figure 13 shows, the lift coefficient for the NACA0009 airfoil aligned and not aligned with the grid converges to an accurate value of 0.4 for an angle of attack of 4 degrees. This correct convergence occurs due to a well defined grid, especially in the vicinity of airfoil.

In the next chapter the effects of rotation on the flow around the airfoil are considered.

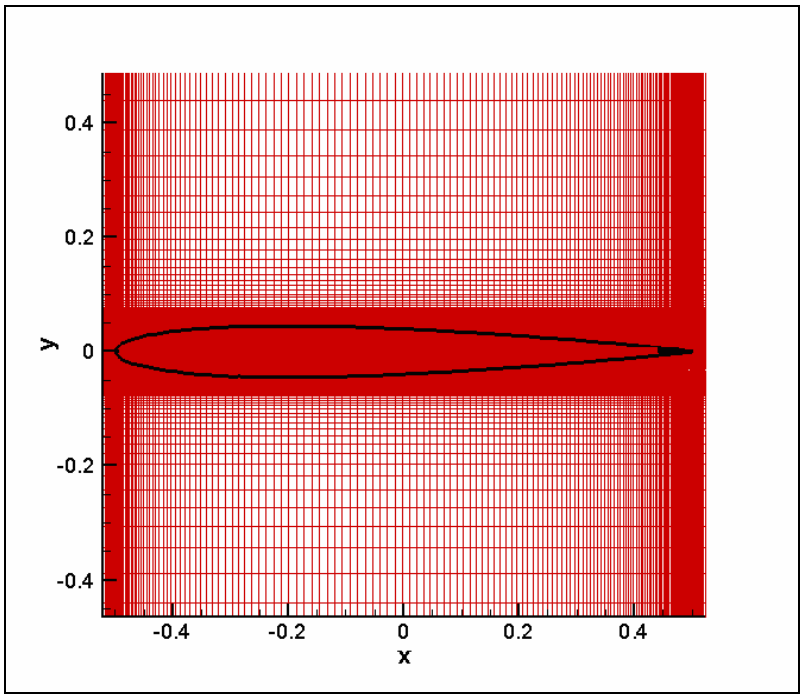

Figure 7 NACA0009 airfoil is aligned with grid

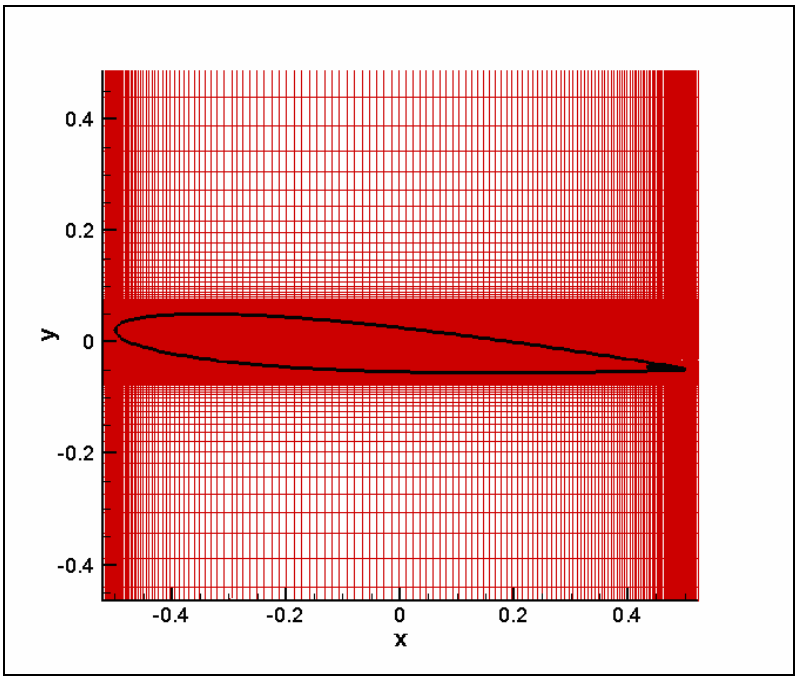

Figure 8 NACA0009 airfoil is set at angle with respect to thegrid

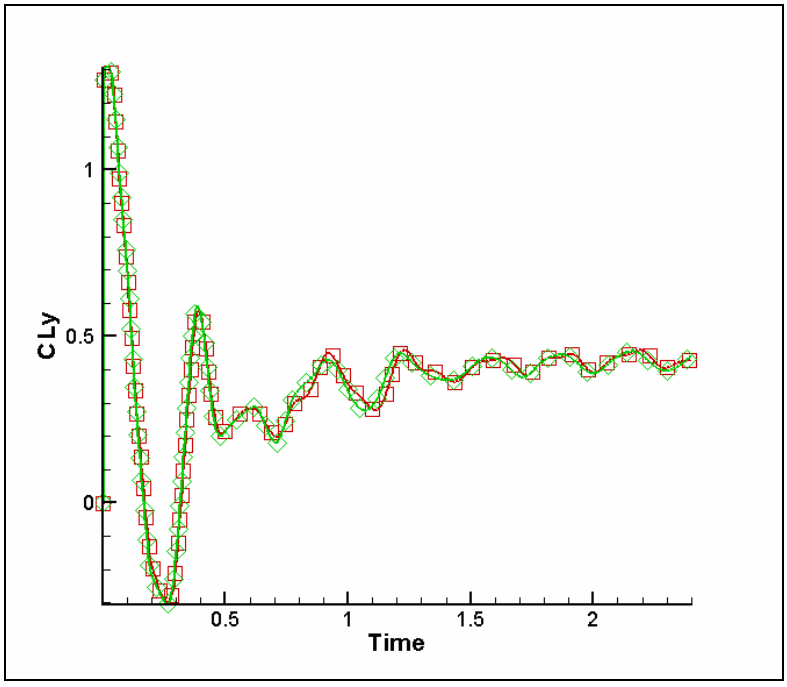

Figure 9 Lift coefficient comparison for stationary case (red) and translating case (green), airfoil aligned with grid

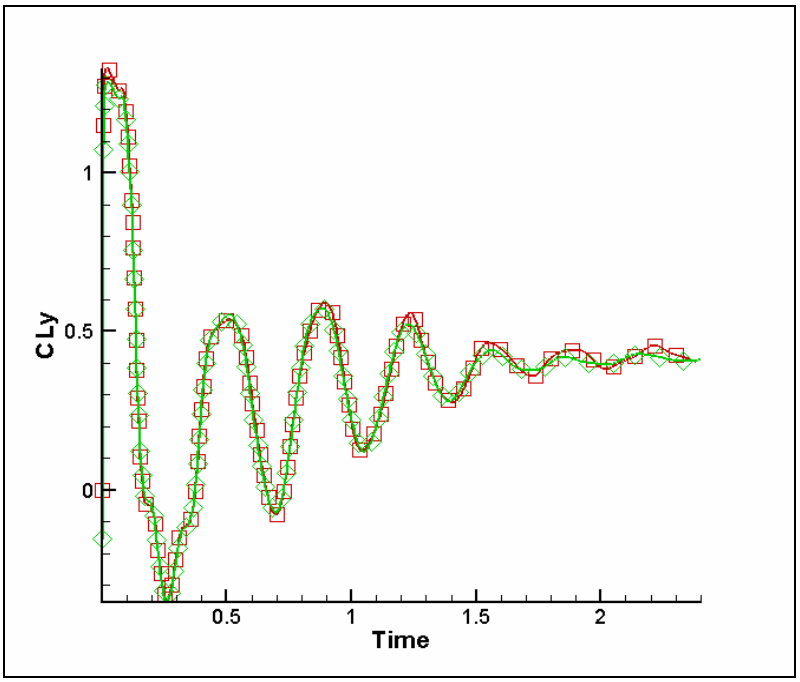

Figure 10 Lift coefficient comparison for stationary case (red) and translating case (green), airfoil at angle with respect to grid

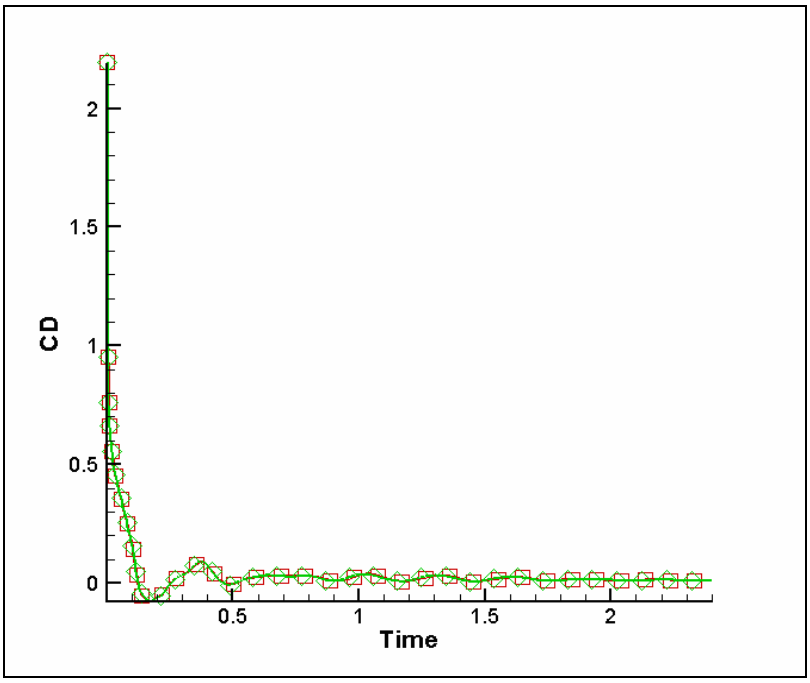

Figure 11 Drag coefficient comparison for stationary case (red) and translating case (green), airfoil aligned with grid

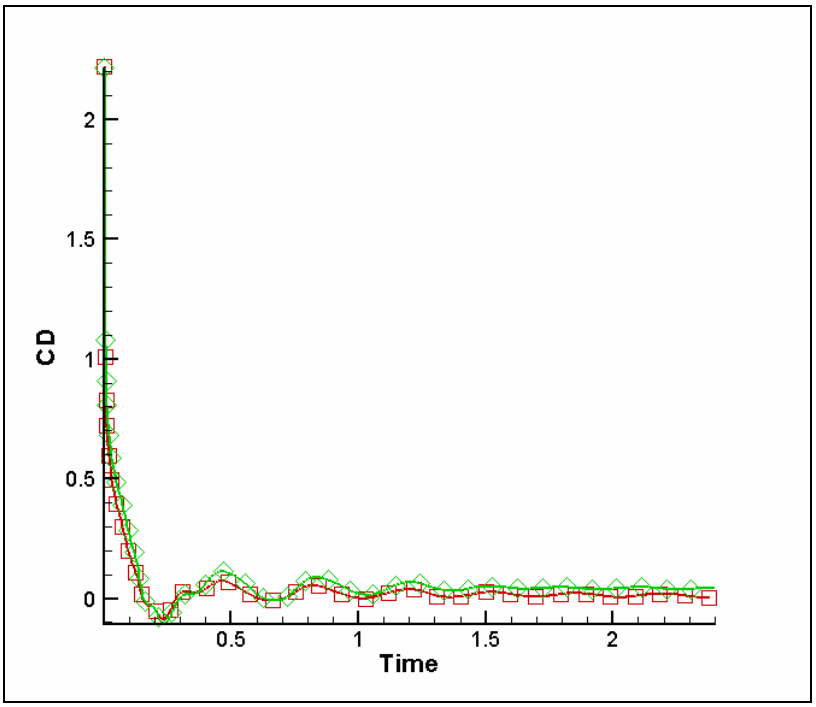

Figure 12 Drag coefficient comparison for stationary case (red) and translating case (green), airfoil at angle with respect to grid

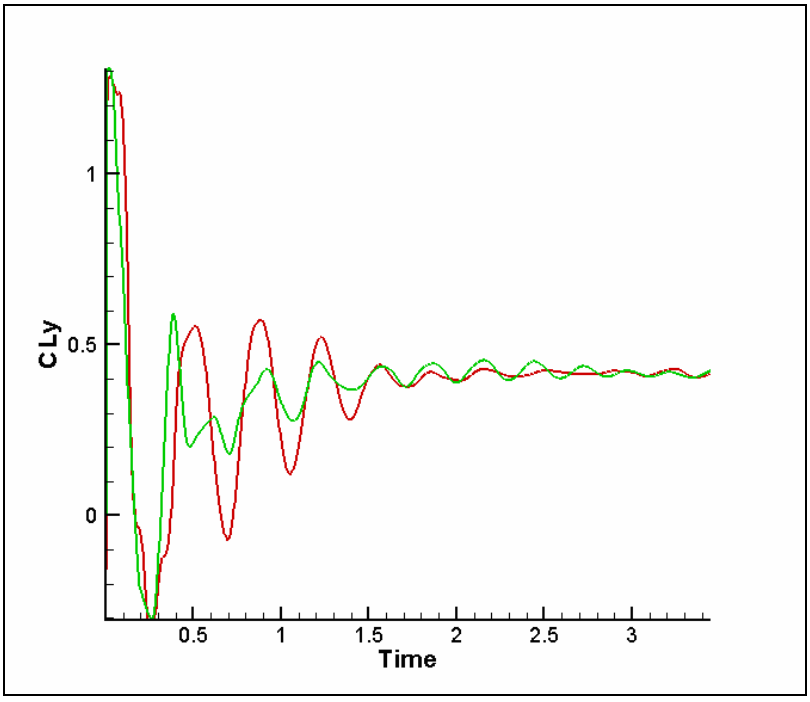

Figure 13 Lift coefficient comparison for translating airfoil, airfoil aligned with grid (green) and airfoil at angle with respect to grid (red)

4

Rotating Blade Simulations

In this chapter, flow analyses are performed for one rotating blade in two cases. In the first, the point of rotation is set far away from the blade. In the second, the point of rotation is moved closer to the blade. For both cases, a moving coordinate system is initiated in order to reduce grid size and computational time. Hence, defined velocities are that of the body and the grid. Just as in the validation cases described in chapter 3, length is non-dimensionalized with respect to the chord of the airfoil, L^* and velocity with respect to speed of sound, a^*.

Point of rotation far away from the blade

The first case for a rotating blade in a quiescent medium is performed by setting the point of rotation far away from the blade. This condition is expected to mimic the flow of a linearly translating blade. Hence, if all initial parameters for both rotating and translating blades are the same, the flow solutions should be nearly identical.

For both cases, an untwisted and untapered blade with a NACA 0015 profile is set at a geometric angle of attack of 4 degrees. The stretched grid dimensions are 293x322x51 in x, y, and z directions respectively, with corresponding minimum values: $\Delta x_{\min} = 0.001c$, $\Delta y_{\min} = 0.0005c$, and $\Delta z_{\min} = 0.015c$. The domain is set to $-10.0c \le x, y \le 10.0c$ and $0.0c \le z \le 4.0c$. The airfoil is set in the middle of the domain.

The chord of the blade is one and is positioned at $-0.5c \le x \le 0.5c$. The span of the blade is two and is positioned at $1.0c \le z \le 3.0c$.

For the rotating case, the point of rotation is set at $z = 18.0$, and the blade rotates with non-dimensional angular velocity of 0.012. For the translating case, the blade translates in the negative *x*-direction with non-dimensional velocity, $u = -0.2$ (relative velocity or the flow velocity is $u = 0.2$). The value of 0.2 is chosen for velocity because the tangential velocity at the mid span of the rotating blade is approximately 0.2 ($u_{\tan} = \omega \cdot r = 0.012 \cdot 16 = 0.192$).

In order to reach a steady state solution, the rotating and translating blades need to travel some distance so that the flow can develop completely. Hence, to reduce complexity of the grids generated, and to reduce the computational effort, a moving coordinate system is incorporated for each case. Therefore, for each case, the grid is either rotating or translating with the same defined velocity as the geometry.

Numerical solutions show that both cases are very similar. Figures 14 and 15 compare the lift and drag coefficients. Even though the curves are not identical due to unsteadiness of the flow, they are very close. Also Figure 16 shows the comparison between the numerical and theoretical lift coefficients. Both curves match reasonably well. Therefore it can be concluded that the flow solution in this case is correct. Appendix B contains a detailed description of the theoretical lift calculations for both the rotating and translating cases.

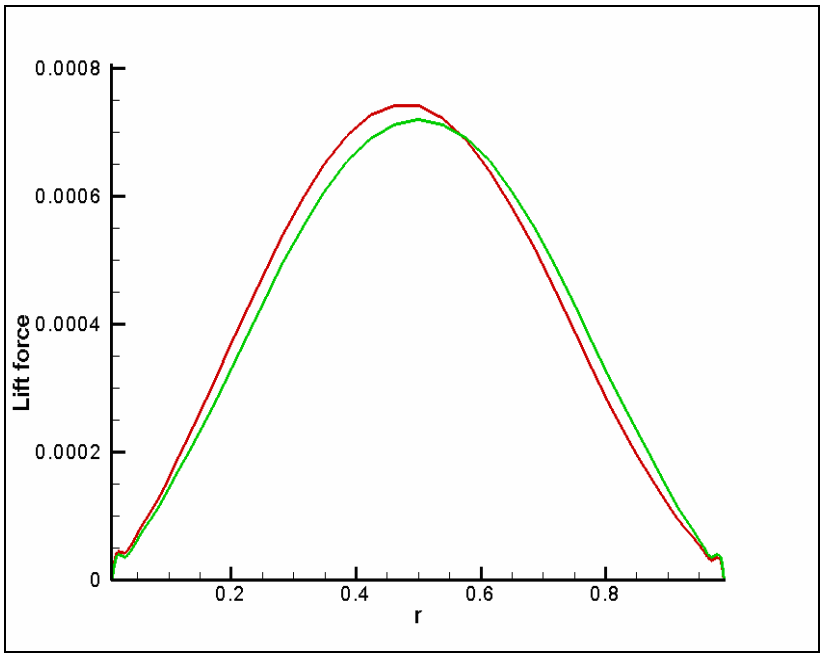

Figure 14 Lift force along the blade span for rotating blade with point of rotation far away from the blade (green) and for translating blade (red)

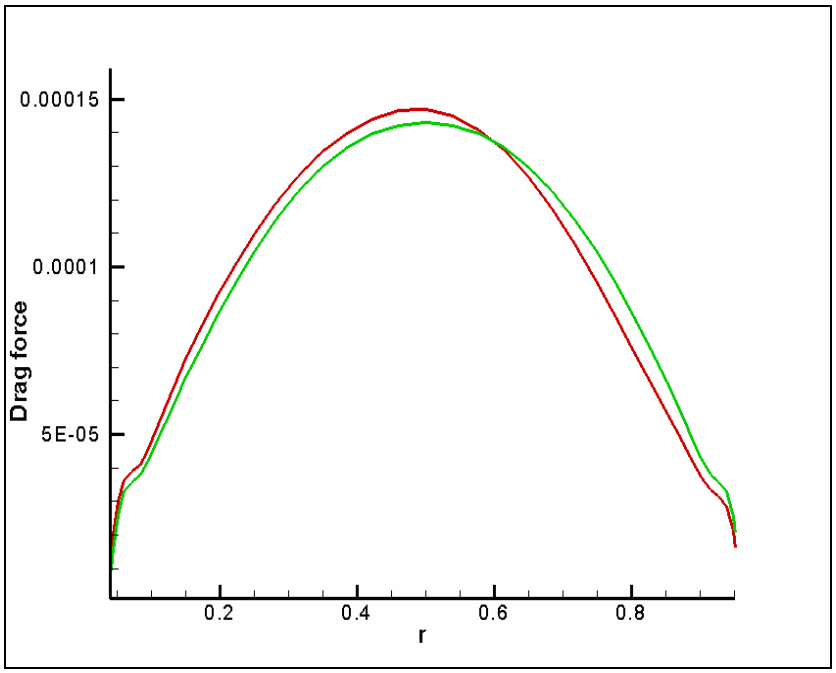

Figure 15 Drag force along the blade span for rotating blade with point of rotation far away from the blade (green) and for translating blade (red)

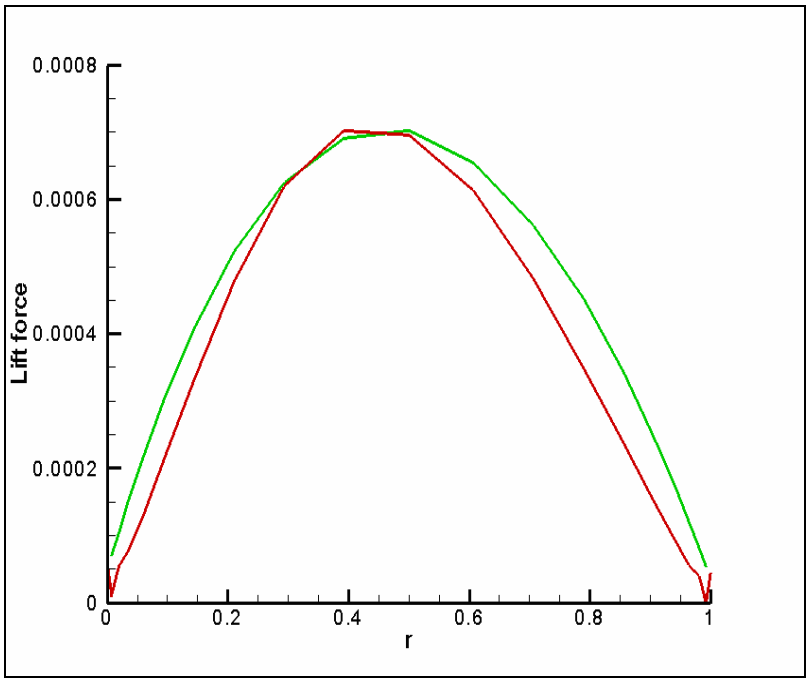

Figure 16 Lift force comparison along the span for the rotating blade, numerical solution (red), theoretically calculated solution (green)

Point of rotation close to the blade

In the second case for a rotating blade, the point of rotation is moved closer to the blade. Hence in this case, the velocity along the span of the blade varies greatly and much more time is necessary for the flow to develop and converge to a steady state.

In order to accurately predict the lift distribution along the span of the rotating blade, it is important to determine the effect of the tip vortices. In hover, the tip vortices coil downward beneath the rotor where they interlock and interact in helical trajectories. As a result, these vortices induce strong velocities, which, in turn, define the net flow velocity at the plane of the rotor and in the rotor wake.[2] Consequently, induced velocities significantly alter the effective angle of attack by "pushing" down on the blades. Reduced effective angle of attack decreases the lift generated by the rotor. For this reason, studying and predicting the strengths and locations of the tip vortices is an essential part in determining the aerodynamic loads on a rotor or a blade.

Boelens et al.[22] and Hariharan et al.[23] in their research papers on rotor wake modeling state that it takes more than one revolution to accurately capture the tip vortex for a rotor with two blades. In this particular case only one blade is rotating. Therefore it would take more than one revolution to simulate a well developed tip vortex and induced velocity though the disk area.

A large number of grid points is necessary in the vicinity of the blade to properly capture the flow and any forming vortices. This is disadvantageous because more computational time is needed for the simulation. In this case, the stretched grid has 331x232x51 points in the *x*, *y*, and *z* directions respectively. The minimum values used for stretching of the grid are $\Delta x_{\min} = 0.003c$, $\Delta y_{\min} = 0.0025c$ for the bottom half of the blade, $\Delta y_{\min} = 0.0001c$ for the top half of the blade, and $\Delta z_{\min} = 0.015c$. The computational domain is set to $-5.0c \le x, y \le 5.0c$ and $0.0c \le z \le 4.0c$. As in the previous case, an untwisted and untapered blade with a NACA 0015 profile is set at a geometric angle of attack of 4 degrees. Also, the airfoil is set in the middle of the domain. The chord of the blade is unity and is positioned from $-0.5c \le x \le 0.5c$. The span of the blade is two and is positioned from $1.0c \le z \le 3.0c$. The point of rotation is moved closer to the blade and is set at $z = 5.0$. A moving grid is also used in this case, so that the blade and the grid rotate with a non-dimensional angular velocity of $\omega = 0.04$.

The 3D CARIBOU code is used for computations. 32 processors are used in the calculations with a local time step for which $dt_{\min} = 7.444 \times 10^{-4}$. For each time step, the blade rotates approximately 0.0017 degrees. After 4.22 days (101.28 hours, 7500 time steps) of run time, the blade rotates 12.77 degrees. Based on these numbers, it is estimated that it would take over 200,000 time steps or over 60 days for the blade to complete one revolution. Such a long computation time makes this rotating blade case unfeasible.

Nevertheless, some analysis of the flow generated has been performed with the limited data collected from the code. The lift force distribution along the blade span is calculated for a single time step and compared with the theoretical prediction in Figure 17. As can be observed, the lift distribution calculated by the code oscillates about the theoretical curve (refer to Appendix B for the theoretical calculations). This is because

after 12 degrees of rotation, the flow is not nearly fully developed. As can be seen in Figures 19 - 28 (the break in the blade is the processor boundary), the tip vortices are small and inconsistent even for the last recorded output.

Figure 18 shows the lift coefficient convergence for this rotating blade. It also shows the average lift coefficient which corresponds to $C_{Laverage} = 0.11$. The total lift coefficient for the theoretical lift distribution also equals to 0.11, which means that the theoretical lift curve is the average of the lift curves plotted in Figure 17. Therefore, it can be concluded that, as time progresses and the flow develops, the lift distribution along the blade radius will get closer and closer to the theoretically calculated distribution, and an accurate flow representation for a rotating blade will be achieved.

In the next chapter the flow generated by a pressure jump in a duct is considered. This is an initial attempt to simulate the flow in a ducted rotor.

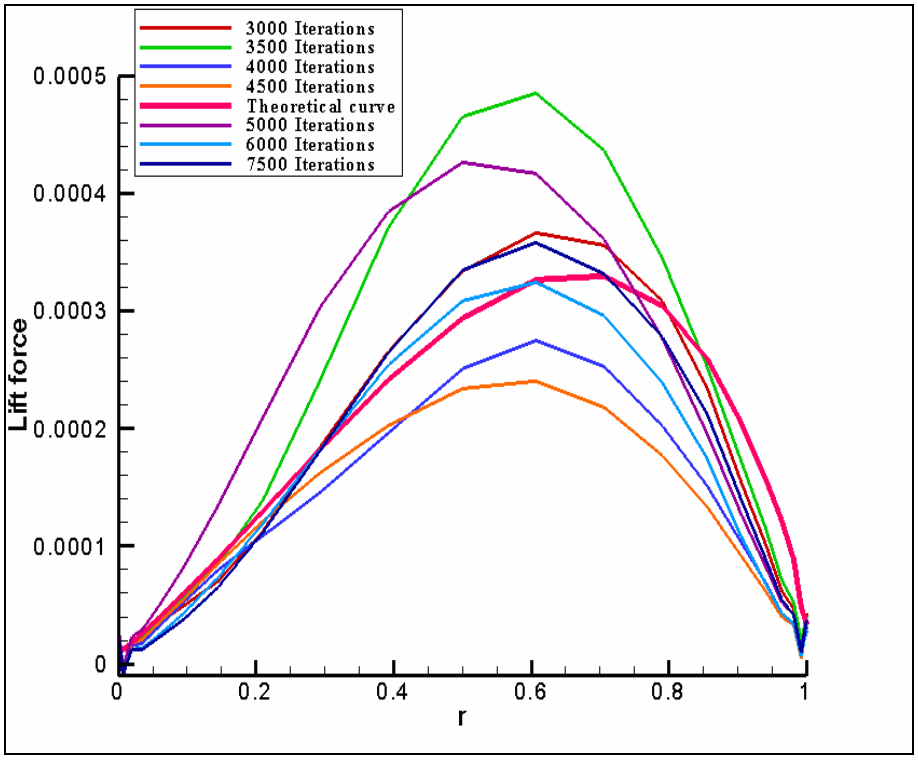

Figure 17 Lift force comparison along the span for the rotating blade. Theoretically calculated lift distribution is represented by pink curve.

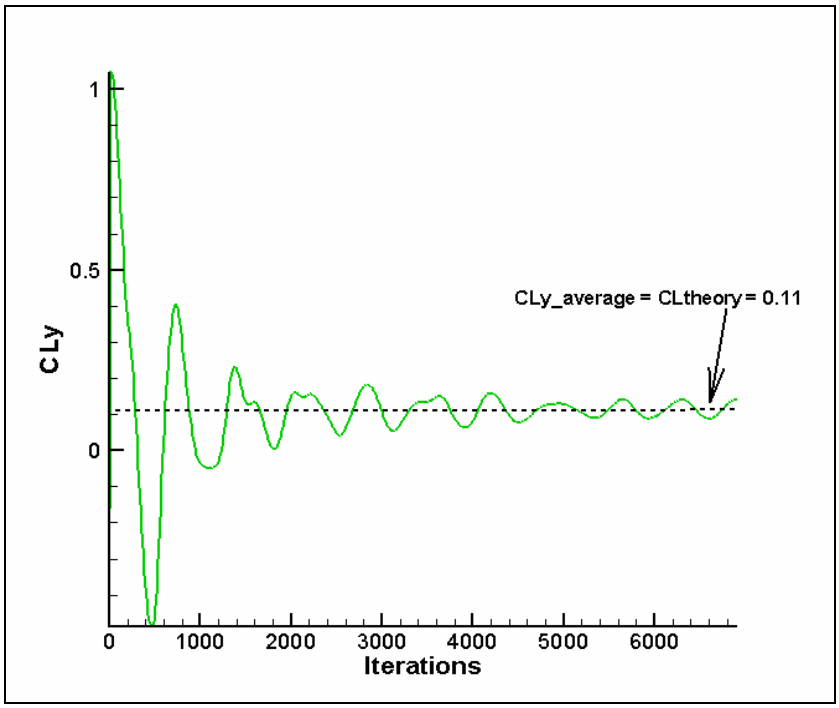

Figure 18 Lift coefficient for the rotating blade. Dashed line represents the average lift coefficient

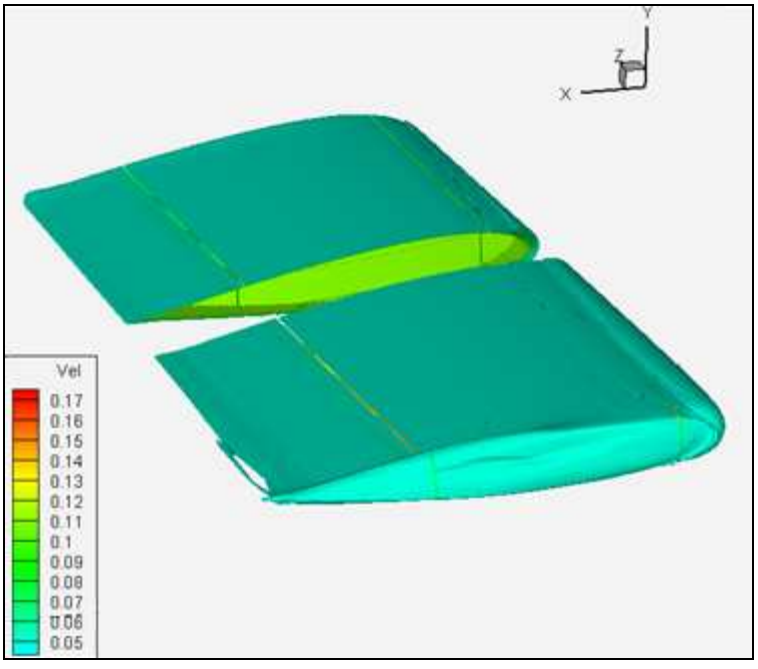

Figure 19 Tip Vortex at 3000 Iterations, azimuth angle, $\psi = 5.11^{\circ}$

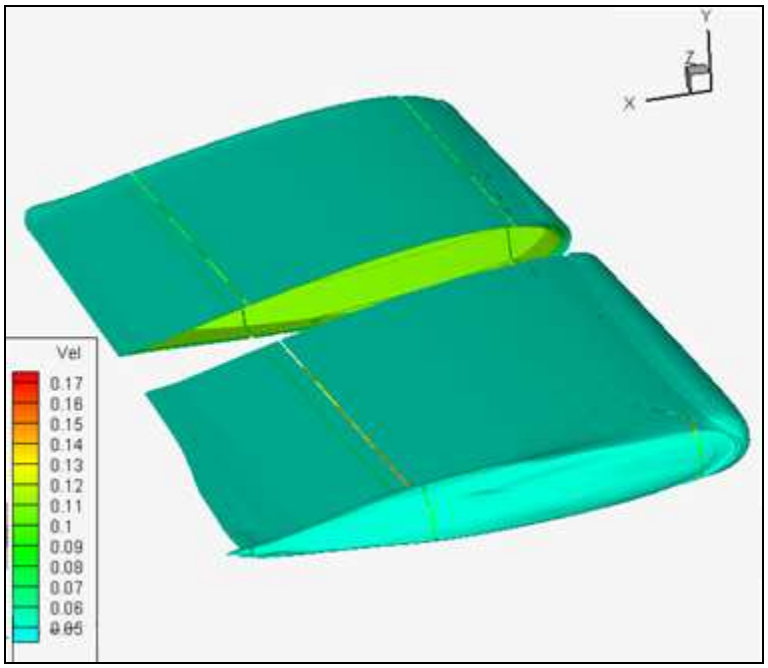

Figure 20 Tip Vortex at 3500 Iterations, $\psi = 5.96^{\circ}$

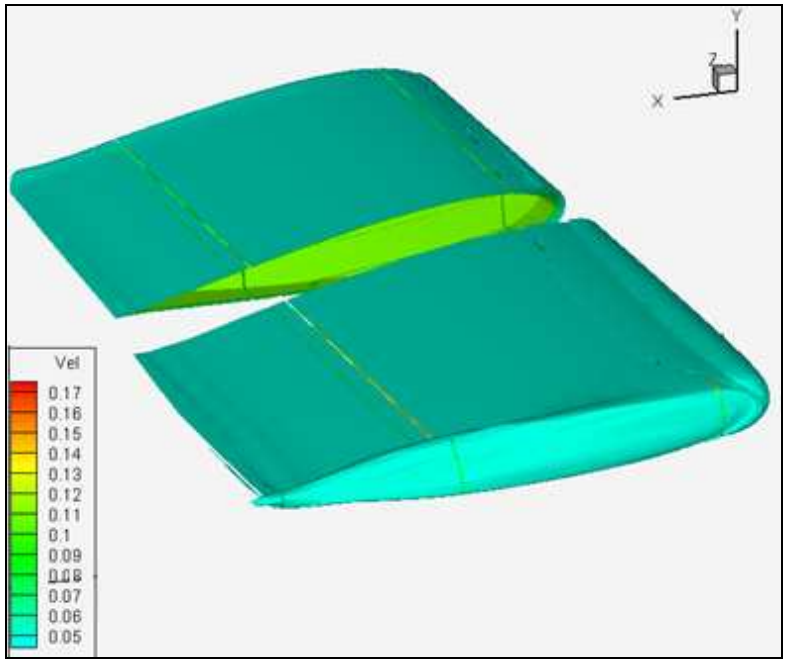

Figure 21 Tip Vortex at 4000 Iterations, $\psi = 6.82^{\circ}$

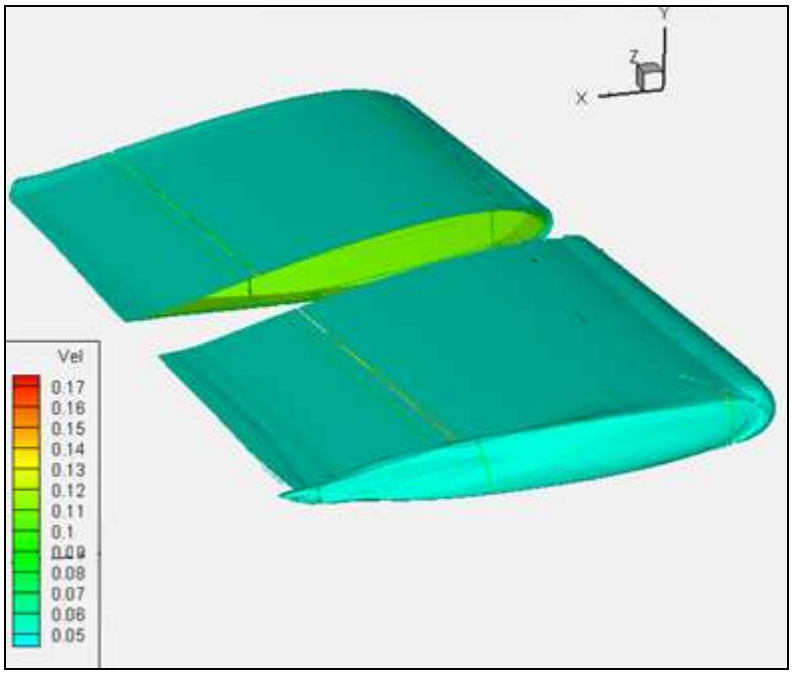

Figure 22 Tip Vortex at 4500 Iterations, $\psi = 7.67^{\circ}$

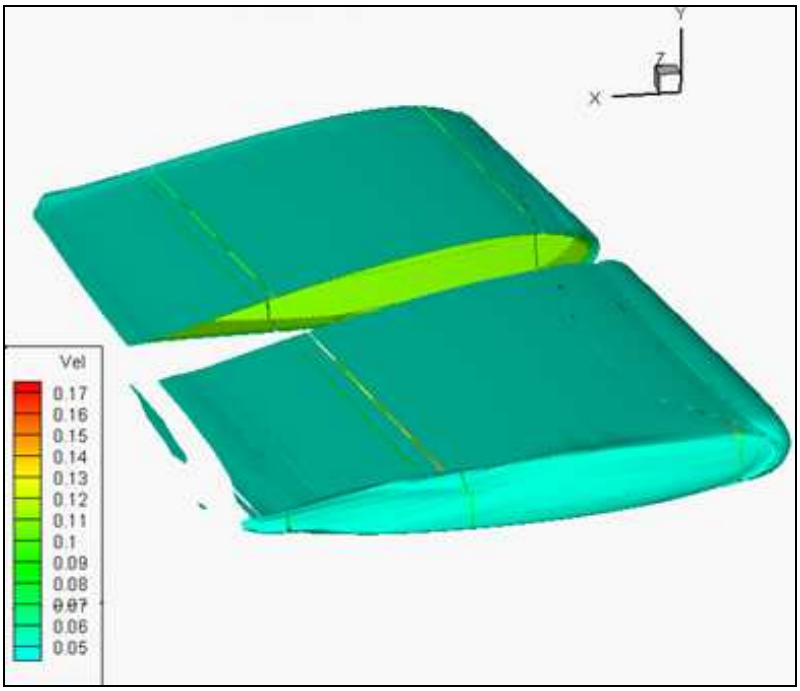

Figure 23 Tip Vortex at 5000 Iterations, $\psi = 8.53^{\circ}$

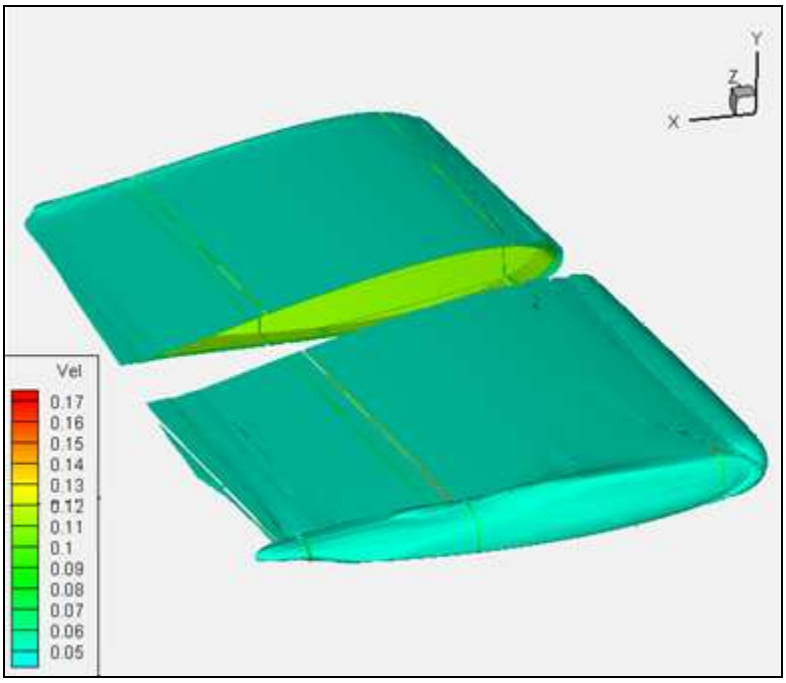

Figure 24 Tip Vortex at 5500 Iterations, $\psi = 9.37^{\circ}$

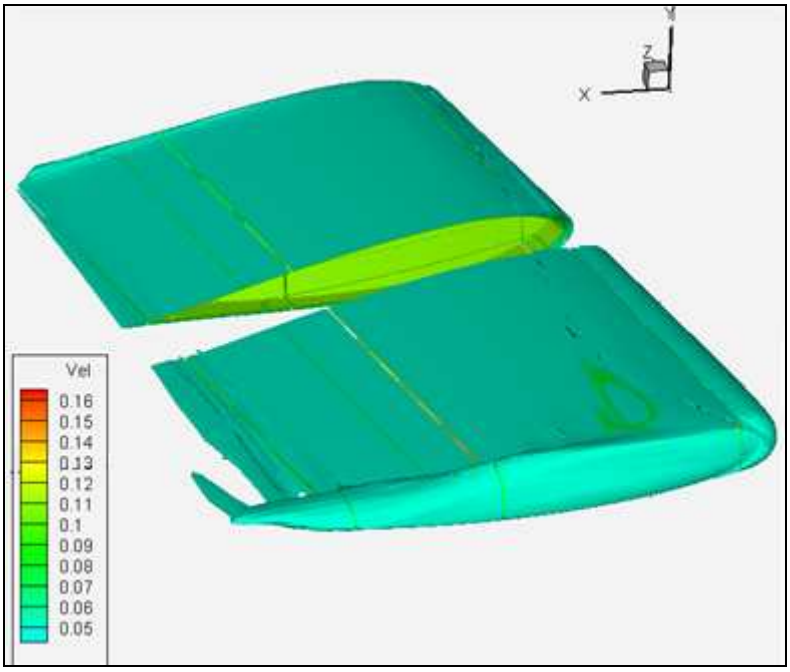

Figure 25 Tip Vortex at 6000 Iterations, $\psi = 10.2^{\circ}$

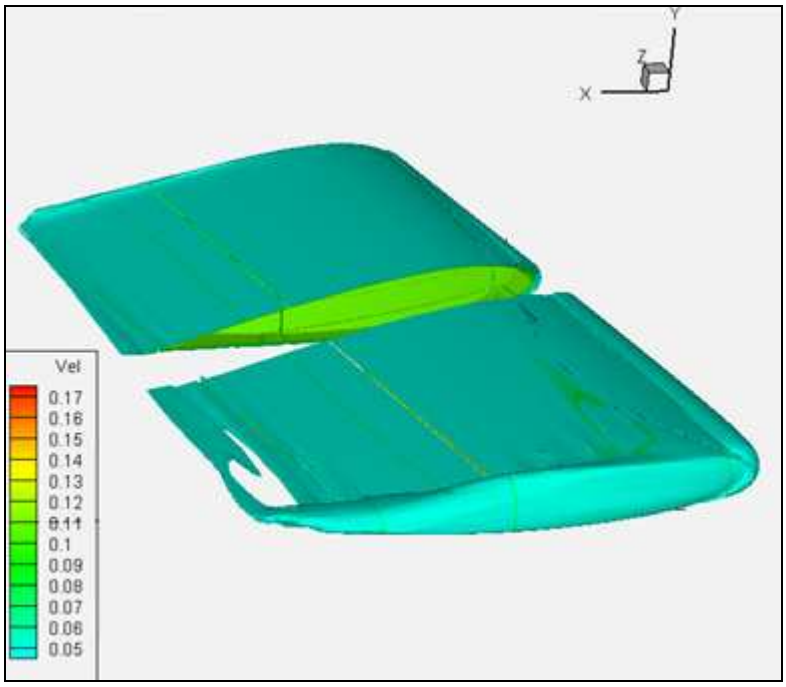

Figure 26 Tip Vortex at 6500 Iterations, $\psi = 11.08^{\circ}$

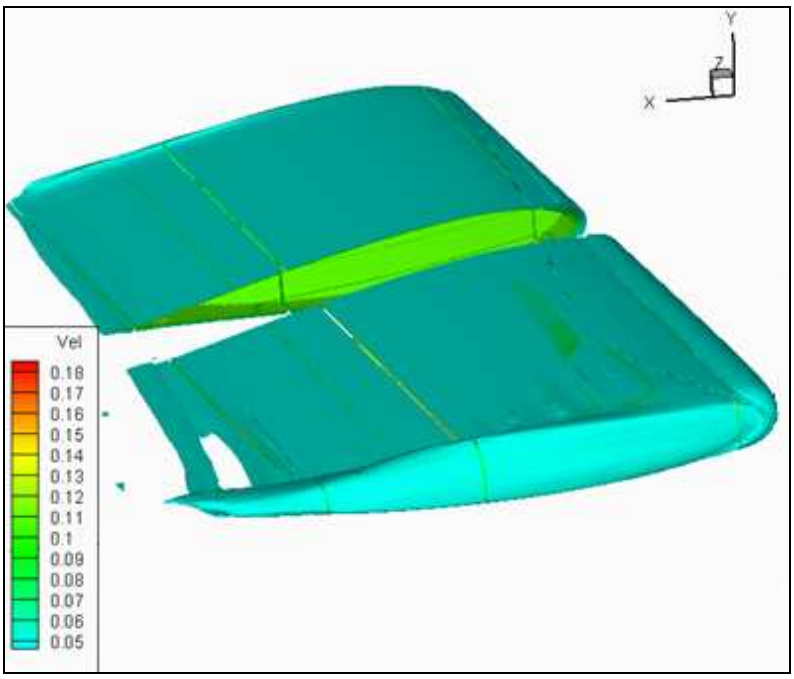

Figure 27 Tip Vortex at 7000 Iterations, $\psi = 11.9^{\circ}$

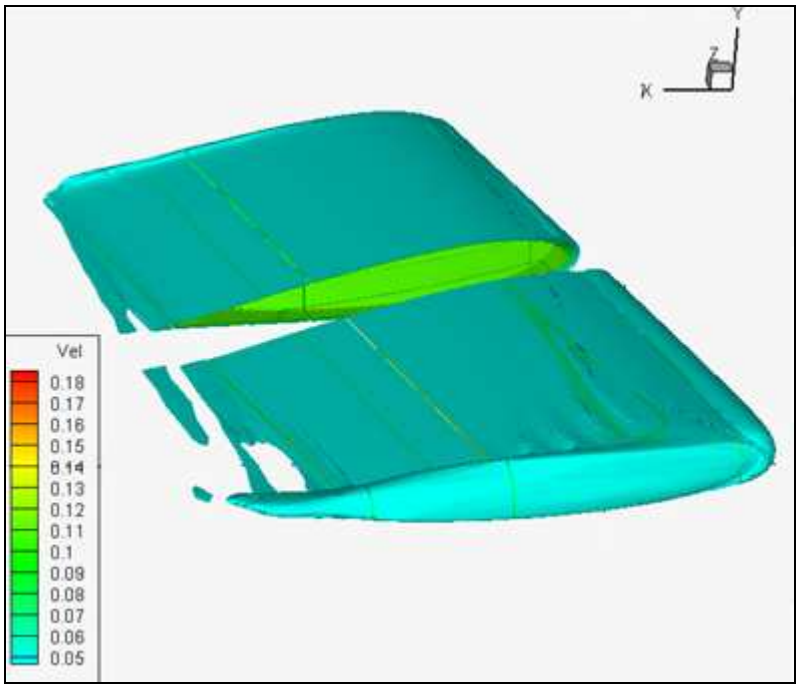

Figure 28 Tip Vortex at 7500 Iterations, $\psi = 12.8^{\circ}$

5

Pressure Jump in a Duct

The CARIBOU code has also been used to simulate the effect of a pressure jump in a duct in order to study how the shape of the duct influences the downwash wake. Since the rotating blade case requires a lot of time for calculations, adding a duct to a problem would only complicate the process and increase the computational time even more. Hence, it is decided that a simpler way of studying flow through a duct is to use a method that has been proven to work in numerous other CFD simulations. This method is to initiate a pressure jump inside the duct in place of a rotating fan.

A simple momentum theory is used to define the pressure discontinuity. Using equations from Leishman's 2nd edition "Principles of Helicopter Aerodynamics", the pressure just above the rotating fan is defined as:

$$p_1 = p_\infty - \frac{1}{4}\frac{T}{A}$$

where, $\frac{T}{A}$ is the rotor disk loading. T is the thrust and A is the disk area. Similarly, the pressure just below the rotating fan is:

$$p_2 = p_\infty + \frac{3}{4}\frac{T}{A}, \text{ hence } \Delta p = p_2 - p_1 = \frac{T}{A}$$

By simply picking a value for Δp, the pressure above and below the rotor disk can be found.

A specific duct geometry has not been identified for this project. Therefore, several shapes are generated. However, for discussion purposes, only three of them are described in detail. The 2D serial version of CARIBOU is used for a quick estimate of the flow behavior as it passes through and exits the duct. In the 2D code, only the cross section of a duct is defined.

The first duct geometry considered is very simple. The cross section consists of two rectangles, see Figure 29. The grid for this case is coarse, 100x100 for the dimensions in the x and y directions, respectively. The domain is $-5.0 \le x, y \le 5.0$ with $\Delta x_{\min} = \Delta y_{\min} = 0.05$. The width of each rectangle is 0.5 and the length is 1.0. The distance between the rectangles, also the width of the duct is 1.0. A non-dimensional pressure discontinuity of $\Delta p = 0.4$ is defined in the middle of the duct, $x = 0.0$. Initially, the medium throughout domain is quiescent. Therefore, as the pressure gradient begins to draw flow through the duct, vortices form at the exit and flow circulates around the duct, see Figure 30. However, this phenomenon gradually dissipates as time progresses, as shown in Figure 31. Due to the uniformly thick cross section of the duct and the sharp corners, vortices continuously form at the exit and move downstream. Since vortices do not shed symmetrically, the wake begins to oscillate vigorously, as can be observed in Figure 32. Hence it is preferred to round these corners so that flow in the wake would appear smoother and straighter.

The second duct cross section consists of two symmetrical airfoils with thickness of 0.08 and the distance between them of 0.04, Figure 33. This geometry is chosen because of the rounded corners at the inlet and an expansion of angle of approximately three degrees at the exit of the duct. Due to the thickness, a finer grid is generated for this case, 180x159 in the x and y directions, respectively, in the domain of $-2.0 \le x \le 5.0$, $-2.0 \le y \le 2.0$ with $\Delta x_{\min} = 0.01$ and $\Delta y_{\min} = 0.004$. The pressure jump is simulated just like in the previous case, except that non-dimensional $\Delta p = 0.5$. Thin ducts are mostly used for high speed fans, hence disk loading is high.[24] As in the first case, vortices form at the exit and flow circulates around the duct, Figure 34. However, in this case, the vortices develop symmetrically. Figures 35 and 36 show that as time progresses, vortices progress down the wake and contract somewhat the wake.

For some cases, this wake narrowing can cause separation of flow from the inner duct walls, because the pressure gradient outside of the duct is not high enough to pull the two vortices apart.

After examining the flow through the two duct shapes described above, it is decided to combine the two geometries together for the third case, by keeping the wide intake surface from the first case, rounding the inlet corner and gradually reducing the thickness of the walls all the way to the exit as in the second case. This is shown in Figure 37. The duct is also set to have an expansion angle of three degrees. This type of duct is mostly used for low fan velocities.[24] However, for a consistent comparison with the thin duct case, the disk loading is kept the same for the third case. That is, $\Delta p = 0.5$.

In the third case, the distance between the shapes is 1.0. The grid used for calculations is 180x221 in the x and y directions, respectively, and the domain is $-2.0 \le x \le 5.0$, $-2.0 \le y \le 2.0$ with $\Delta x_{\min} = \Delta y_{\min} 0.01$. The non-dimensional pressure jump of $\Delta p = 0.5$ it is set at $x = 0.0$. The early stages of flow development are similar to the ones described in the previous cases, as shown in Figure 38. However, due to the higher pressure gradient outside of the duct (the pressure gradient is higher because of the duct geometry) the vortices are smaller and are farther apart. This is shown in Figure 39. Although the wake contracts down stream, the flow at the exit expands more than for the thin duct case, as shown in Figure 40.

It should be noted that the expansion angle in the last two cases is kept under four degrees. If the diffusion angle is too large at the outlet, the flow will separate.

It can be concluded that the geometry of the duct influences the downstream wake and hence the aerodynamic loads produced on the ducted fan system. Many more studies can be performed on the shapes of the duct using the CARIBOU code and additional in depth analysis can be executed.

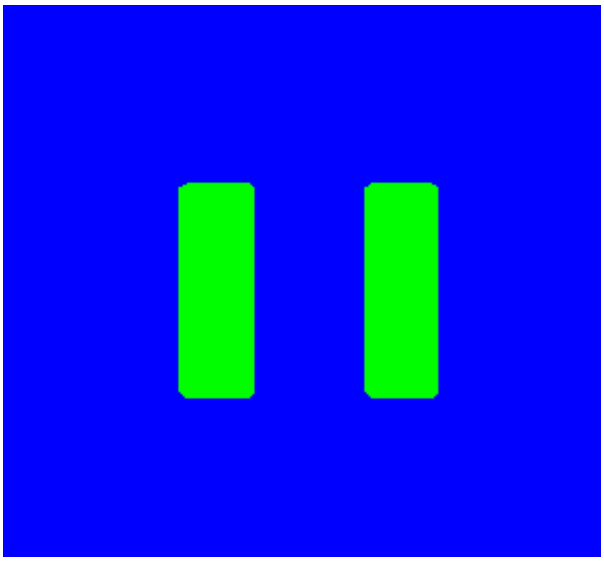

Figure 29 Cross section of the first duct

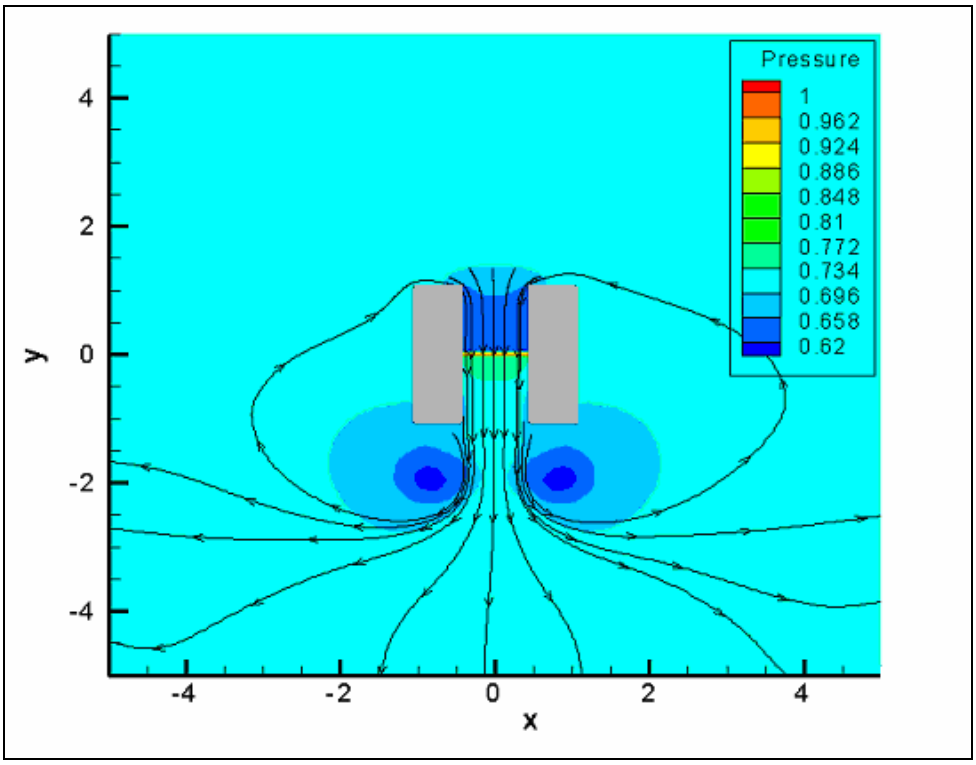

Figure 30 Flow through the duct with cross section of two rectangles, 1000 iterations

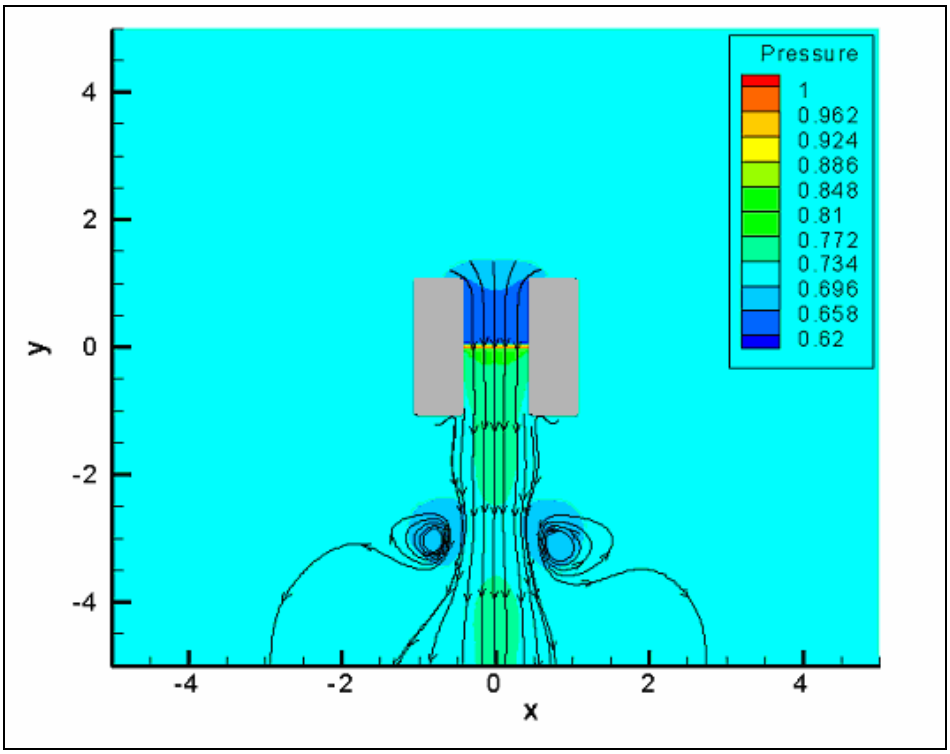

Figure 31 Flow through the duct with cross section of two rectangles, 4000 iterations

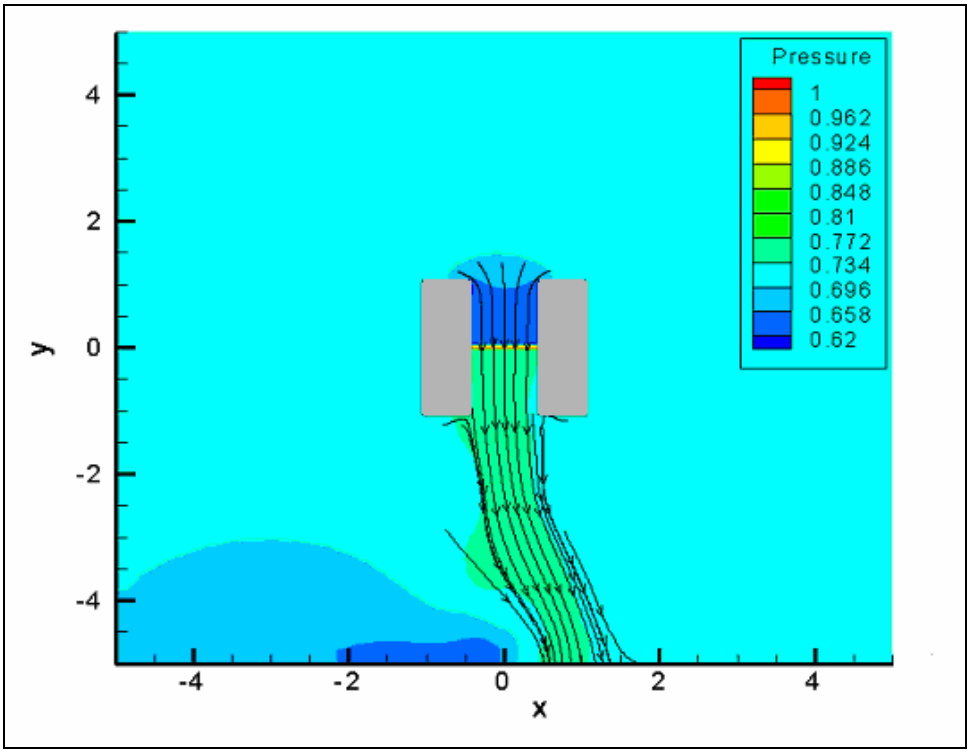

Figure 32 Flow through the duct with cross section of two rectangles, 9000 iterations

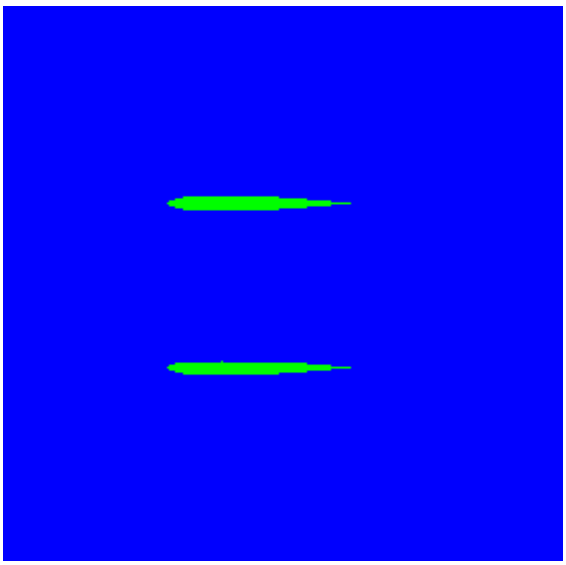

Figure 33 Cross section of the duct

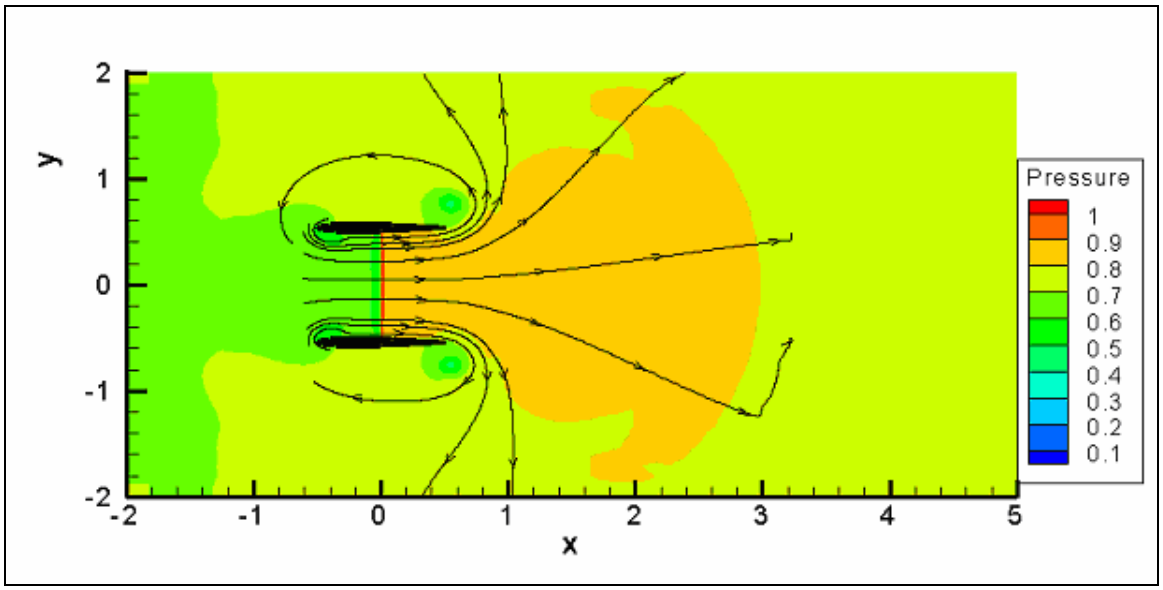

Figure 34 Flow through the duct with cross section of two airfoils, 1000 iterations

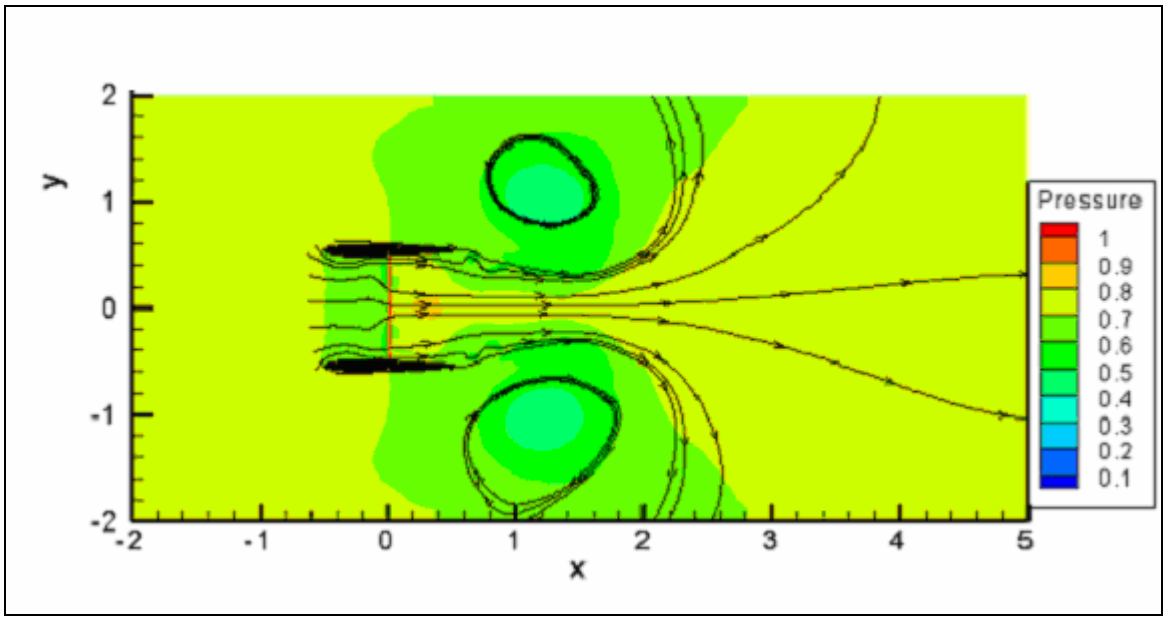

Figure 35 Flow through the duct with cross section of two airfoils, 5000 iterations

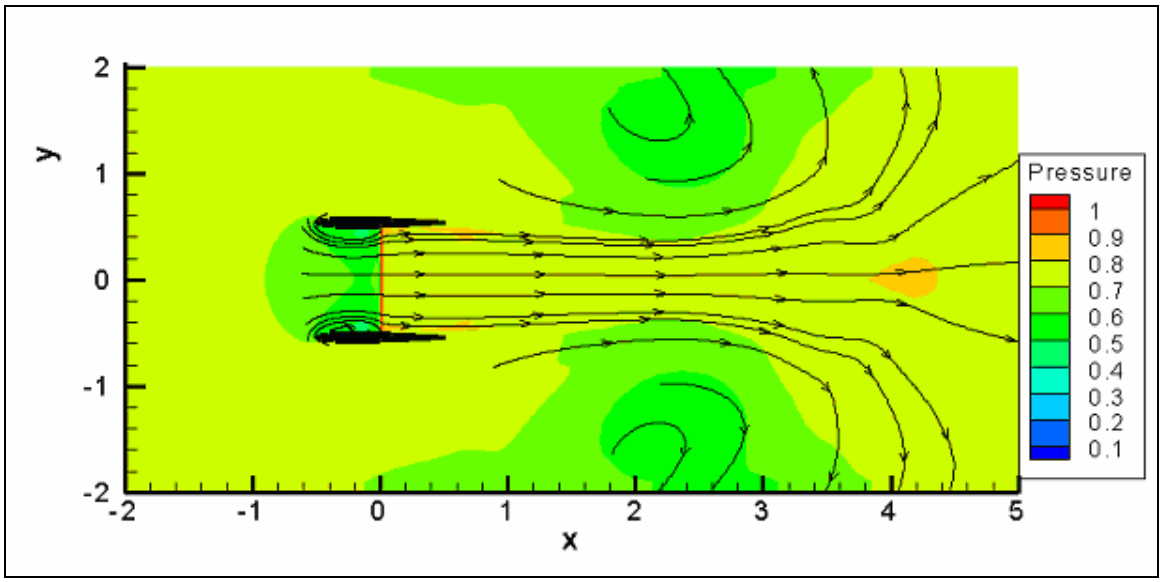

Figure 36 Flow through the duct with cross section of two airfoils, 7000 iterations

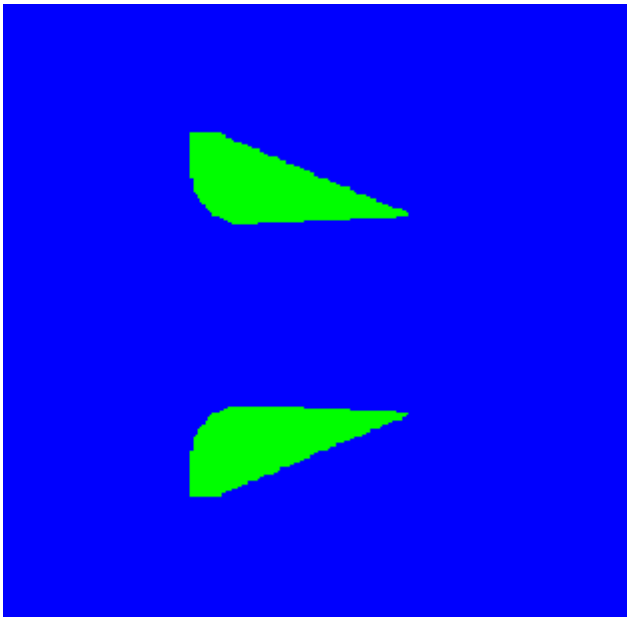

Figure 37 Cross section of the duct

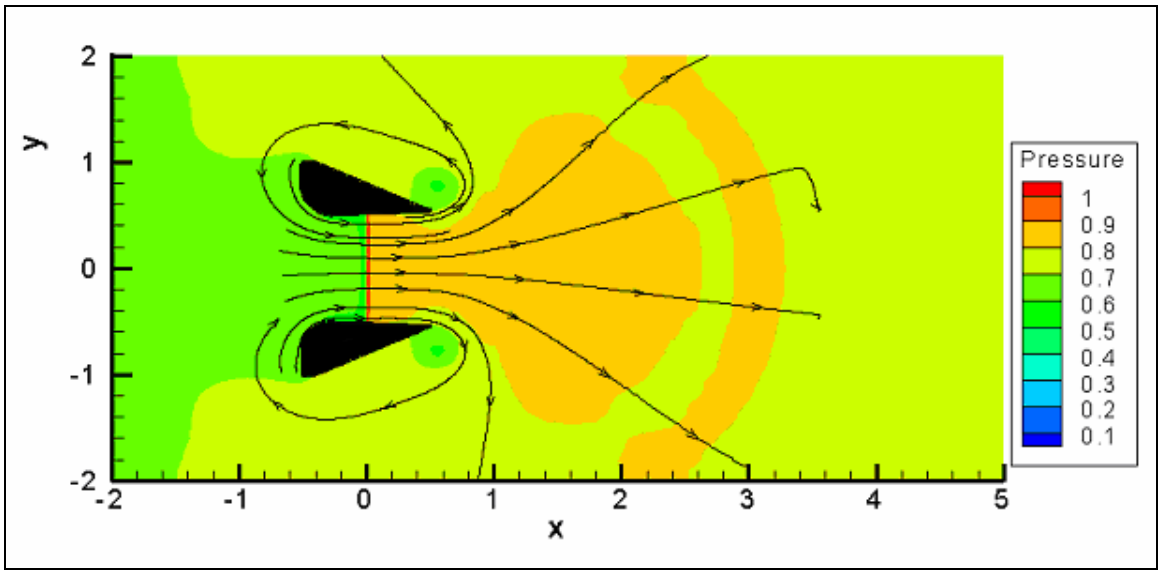

Figure 38 Flow through the duct, 1000 iterations

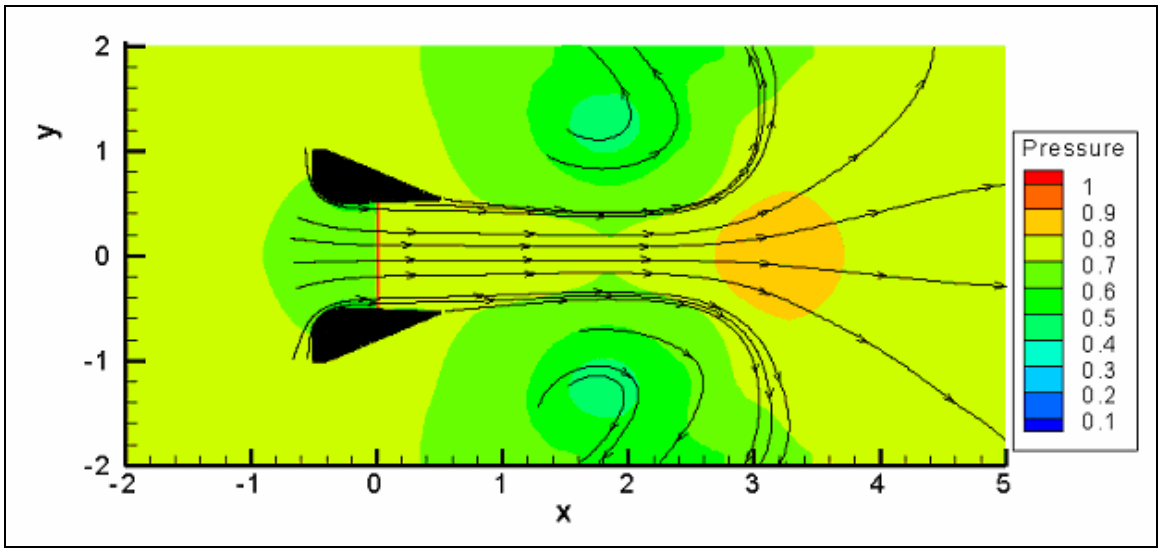

Figure 39 Flow through the duct, 5000 iterations

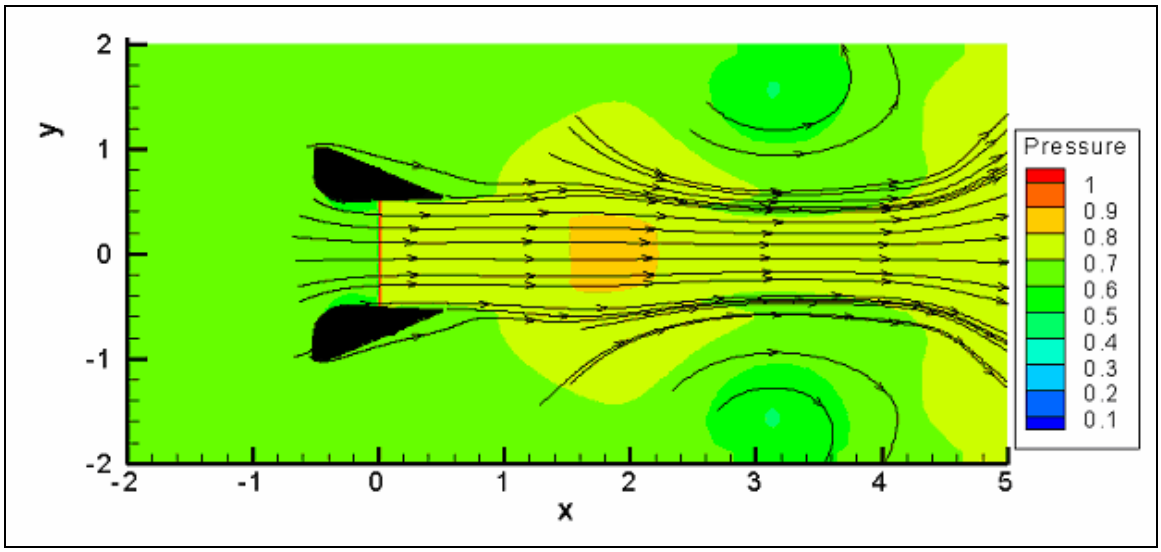

Figure 40 Flow through the duct, 7000 iterations

6

Conclusion/Future Work

The objective of research described in thesis has been to study flow behavior in a ducted fan using the in-house code "CARIBOU". In CARIBOU, computations are performed on a structured Cartesian grid using the immersed boundary method. The code can use either compressible or incompressible Navier-Stokes equations for computations. The 4^{th} order Runge-Kutta method is used for time marching and a Weighted Essentially Non-Oscillatory (WENO) scheme is used for space discretization and to eliminate any unphysical numerical oscillations. In some of the cases, a moving coordinate system is implemented in order to reduce the number of grid points, reduce the domain size, and hence reduce the computational effort.

Several validation cases have been simulated in order to assess the capabilities and accuracy of the CARIBOU code.

- The first validation is a flow simulation in the vicinity of rotating cylinder in a viscous quiescent medium. Velocity plots show that the flow is generated with the correct qualitative features.
- The second validation case is the oscillation of a wall in its plane in a quiescent medium. This problem is called Stokes's second problem. The numerical solution compares well with the theoretical results.
- The third validation studies the relationship between the viscous and inviscid CARIBOU codes. If the grid spacing in the inviscid code is such that,

$\Delta y = \mathrm{Re}^{(-3/4)}$, then the viscous code with that particular Reynolds number calculates the same flow solution as the inviscid code. At least, within the framework of the immersed boundary method. This relationship is particularly helpful when the viscous code becomes too expensive in terms of computational time. This validation is conducted by simulating flow over a short blade with a NACA0009 cross section.

- The fourth validation is performed for moving and stationary coordinate systems. Results show that the calculated flow solution for both cases is the same if all initial parameters are identically defined. The moving grids are beneficial when the defined body has to travel a long distance in order for the flow solution to achieve a steady state. Instead of generating a large grid which would trace the motion of a body, a moving grid need only be as big as necessary to calculate the flow in the vicinity of the body. This comparison is performed by translating an infinitely long blade with a NACA 0009 cross section.

Next, two studies are conducted for an untwisted and untapered blade with a NACA 0015 profile. Both studies use the inviscid, moving grid version of the CARIBOU code.

- The first study compares a rotating blade far away from its point of rotation and a translating blade, with identical initial parameters. The rotating blade far way from its point of rotation has the flow solution which resembles that of a translating blade. Hence, the lift force distribution along the span for both situations is very similar.
- The second study is for a single rotating blade in a quiescent medium. In order to capture the flow around the blade accurately, a large number of grid points is used in the vicinity of the blade. As a result, 32 processors are used in the calculations with $dt_{\min} = 7.444 \times 10^{-4}$. The blade rotates with a non-dimensional angular velocity of 0.04. This means that for each time step, the blade rotates 0.0017 degrees. It would take over 200,000 time steps or over 60 days to complete one revolution. Since more than one revolution is required for accurate flow analysis, this rotating case is unfeasible for this study. However, the collected numerical data shows that for the early stages of flow development, the lift force distribution along the blade span oscillates about the average of the

theoretical lift curve. This is because the tip vortices are small and not yet developed and hence the induced velocity is low and unsteady. However, as time progresses and the flow develops, the lift force distribution should become closer to the theoretical curve.

Since, a full rotating blade study is impractical with the current code, adding a duct to the problem would only further complicate the calculations and increase the computational time. Therefore, a pressure jump inside a duct is simulated in place of the rotor. Three duct geometries are generated and the flow is studied for each.

- The first duct has a cross section of two rectangles. Flow is drawn through the duct by a non-dimensional pressure discontinuity which equals $\Delta p = 0.04$. As the flow develops, vortices form at the outflow due to the sharp corners and large duct surface at the exit. As these vortices move downstream asymmetrically, the wake begins to oscillate robustly. Hence it is preferred to improve the duct geometry to eliminate such strong wake oscillations.
- The second duct has a cross section of two thin symmetrical airfoils. Since thin ducts are mostly used for high speed fans; the non-dimensional pressure jump is increased to 0.5. At the early stages of flow calculation, vortices form at the exit and as time progresses they move down the wake. This translation causes a contraction in the wake.
- The third duct has a large cross section at the inlet and much smaller cross section at the outlet. This duct shape is primarily used for low speed fans. However, in order to compare the flow solution with the thin duct in the second case, the non-dimensional pressure discontinuity is kept at 0.5. The early flow development around the duct is similar to the previous two cases. Due to the high pressure gradient outside of the duct due to the wall inclination, the vortices that form and translate downstream are smaller and seem to be farther apart. However, the vortices still contract the wake. The flow expands more at the duct exit for this duct shape than for a thin duct case.

Some recommendations for future work are to develop a better study for the rotating blade so that less time would be required for computations. Also, a grid with cylindrical coordinates can be developed so that a rotor with several blades can be studied by simulating rotation of one blade with periodic boundary conditions. When that task is accomplished a duct wall can be added to the rotating blade set up to study blade-duct interactions.

Appendix A

Ducted Fan Theory

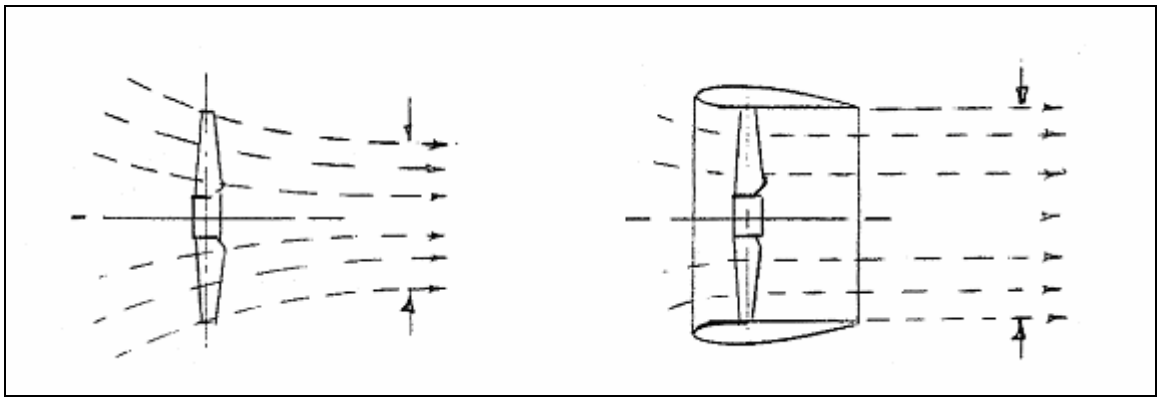

Figure 41 Flow models for an open rotor (left) and ducted rotor (right)[24]

One of the advantages of enclosing a free rotor in a duct is that wake does not contract, see Figure 41. The ducted fan creates an almost constant diameter slip stream which equal to the diameter at the exit. The first theoretical analysis of the ducted fan was attempted by Kruger[4] in 1949 and the first experiments were performed by Mort[5,6] in 1965 and 1967. Momentum theory for an open rotor can be fitted for the ducted fan theory. It should be noted that all equations are taken from Leishman's second edition "Principles of Helicopter Aerodynamics" textbook.

Assuming that the flow far upstream of the duct is zero and the velocity at the rotor plane is the induced velocity, v_i, then the mass flow rate trough the duct system is

$$\dot{m} = \rho A v_i = \rho(a_w A)w,$$

where A is the area at the duct exit, w is the velocity at the duct exit, and a_w is a wake contraction parameter. Hence, it can be defined that $w = \frac{v_i}{a_w}$.

Applying the conservation of momentum to the system, the thrust generated on the duct and fan is

$$T = T_{duct} + T_{fan} = \dot{m}w = (\rho A v_i)w = \frac{\rho A v_i^{\,2}}{a_w}.$$

The induced velocity can also be defined as $v_i = \sqrt{\frac{a_w T}{\rho A}} = \sqrt{\frac{T}{2\rho A_{eff}}}$, where $A_{eff} = \frac{A}{2a_w}$.

According to the momentum theory for an open rotor, the trust produced by the fan is

$T_{fan} = \frac{1}{2}\rho w^2 A$. Hence the ratio between total thrust on the ducted fan and the thrust on

the fan is

$$\frac{T_{fan}}{T} = \frac{w}{2v_i} = \frac{1}{2a_w}.$$

Consequently, the induced power ratio can also be calculated,

$$\frac{(Pi)_{fan}}{(Pi)_{TR}} = \frac{1}{\sqrt{2a_w}},$$

where $(Pi)_{TR}$ is the induced power consumed by an open rotor. The induced power ratio suggests that if the duct has a geometry so that the wake does not contract and $a_w = 0.5$ and $A_{eff} = A$, less power will be necessary to produce given total thrust.[2] If $a_w = 1.0$ and $A_{eff} = A$, 30% less power will be consumed by a ducted fan in order to generate same total thrust.[2] However, if the area of the duct equals half of the area of an open fan, then the ducted fan will produce the same thrust for the same consumed power.[1]

Appendix B

Theoretical Calculations of Lift for rotating and translating blades

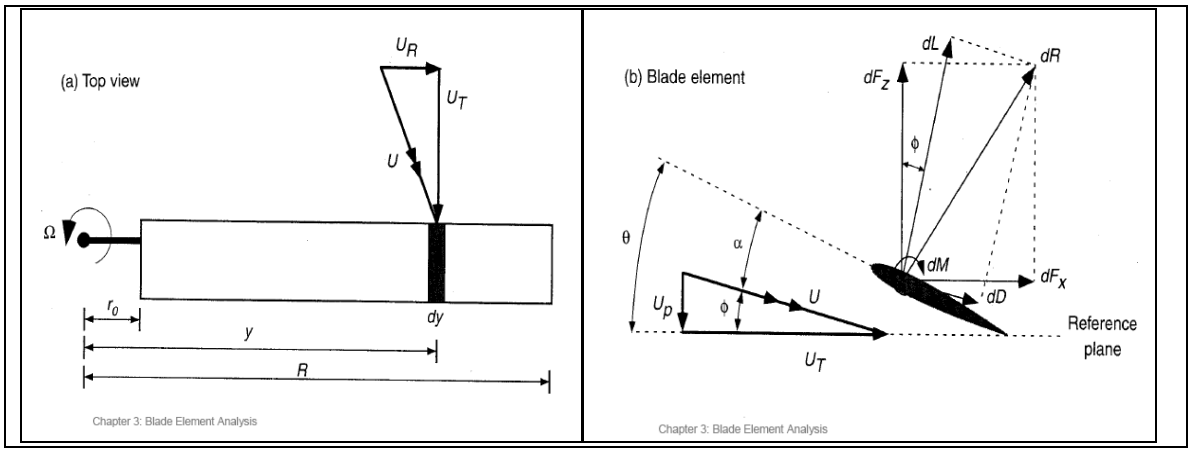

Figure 42 Illustration of aerodynamic forces produced on a blade and airfoil cross section[2]

- **Process for calculating lift for translating blade**

  Before calculations can be performed, initial parameters used in the code are dimensionalized.

  - c* is speed of sound (343 m/s)
  - L* is unit of length (1 meter)
  - P* is pressure at sea level (101,325 Pa)
  - $\gamma = 1.4$
  - $AR = 2$, aspect ratio
  - lift curve slope is 0.1 per degree, therefore $a_0 = 5.73$ [25]

  Chord* = $chordL^* = 1(1m) = 1m$

  $U^* = Uc^* = 0.2(343m/s) = 68.6m/s$

$$\rho^* = \rho \frac{\gamma P^*}{(c^*)^2} = 1 \frac{1.4(101325Pa)}{343^2} = 1.2057 kg/m^3$$

$$Cl_\alpha = \frac{dCl}{d\alpha} = \frac{a_0}{\sqrt{1 + (a_0/\pi AR)^2} + (a_0/\pi AR)} = 2.5295$$

$$\theta = 4^\circ \frac{\pi}{180} = 0.06981$$
$$Cl = Cl_\alpha(\theta) = 0.1766$$

$$dL^* = 0.5(U^*)^2 (chord^*)(\rho^*)(dz^*)\, Cl$$

where, dz is the incremental length which is taken from code and multiplied by 1 meter for dimension.

For comparison with the incremental lift force calculated by code, it is necessary to non-dimensionalize the calculated dL^*:

$$dL = \frac{dL^*}{(c^*)^2 \rho^* (L^*)^2}$$

- **Process for calculating lift for rotating blade**

Assumptions are the same as for the translating blade case.

Chord* = $chordL^* = 1(1m) = 1m$

Length of the blade plus cut-off, $R^* = RL^* = 5.25(1m) = 5.25m$

Angular velocity, $w^* = w\frac{c^*}{L^*} = 0.1\frac{343m/s}{1m} = 34.3 rad/s$

Inflow velocity, $Up = \lambda w^* (R^*)$

where inflow ratio is $\lambda = \frac{\sigma Cl_\alpha}{16}\sqrt{1+\frac{32\theta(r)}{\sigma Cl_\alpha}}-1$ (without tip loss correction factor), where $r = \frac{z*}{R*}$, z is length along span taken from code and multiplied by 1 meter for dimension

$$U* = \sqrt{(Ut*)^2 + (Up*)^2}$$

$$Cl_\alpha = \frac{dCl}{d\alpha} = \frac{a_0}{\sqrt{1+(a_0/\pi AR)^2}+(a_0/\pi AR)} = 2.5295$$

$$\theta = 4^\circ \frac{\pi}{180} = 0.06981$$
$$Cl = Cl_\alpha(\theta) = 0.1766$$

$$dL* = 0.5(U*)^2\,(chord*)(\rho*)(dz*)\,Cl$$

$$dL = \frac{dL*}{(c*)^2\,\rho*\,(L*)^2}$$

When non-dimensionalized theoretical lift force distribution along the blade radius for translating and rotating blades are plotted, it can be observed that they are similar (6% difference between maximum values).

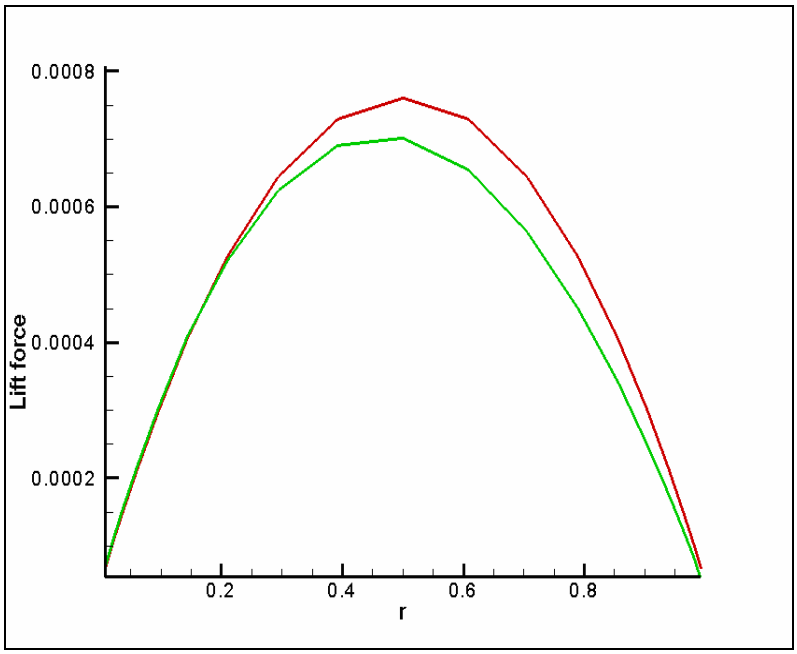

Figure 43 Comparison of theoretical lift force along the blade span for rotating (green) and translating (red) blades

Appendix C

Calculation of the dimensional distance in the oscillating wall case

Exact solution for the oscillating wall examples is:

$$u^*(y,t) = U^* e^{-k^* y^*} \cos(\omega^* t^* - k^* y^*)$$

where, $k^* = \sqrt{\omega^* / 2\nu^*}$ and ν^* is kinematic viscosity

This equation is dimensional and each variable is dimensional, therefore it is necessary to non-dimensionalize each variable with respect to the speed of sound, a^* and arbitrary length, L^*

$$\omega = \omega^* L^* / a^*$$
$$y = y^* / L^*$$
$$t = t^* a^* / L^*$$
$$u = u^* / a^*$$
$$U = U^* / a^*$$

In order to compare the numerical with the theoretical solution, it is required to determine relationship between the dimensional and non-dimensional 'y'.

$$y^* \sqrt{\omega^* / 2\nu^*} = yL^* \sqrt{(\omega a^* / L^*)/(2\nu^*)} = y\sqrt{(\omega/2)(L^* a^* / \nu^*)},$$

But the Reynolds number is, $\mathrm{Re} = L^* a^* / \nu^*$, therefore,

$$y^* \sqrt{\omega^* / 2\nu^*} = y\sqrt{\omega \mathrm{Re}/2}$$

$$y^* = y \frac{\sqrt{\omega \mathrm{Re}/2}}{\sqrt{\omega^* / 2\nu^*}}$$

ω is angular frequency and its value is chosen by a user, y and $v*$ are also known. The only variable that needs to be calculated is $\omega*$.

It is known that angular frequency, $\omega* = 2\pi / T$. If $T = 360$ seconds, then $\omega* = 2\pi / 360$ (radians per second). When non-dimensionalized, $\omega = \omega*(360/2\pi)$, hence $\omega* = 0.01745\omega$. Now all variables are known and the dimensional '*y*' can be calculated using non-dimensional variables calculated by CARIBOU and comparison between theoretical and numerical solutions can be accomplished.

References

[1] Chang, I-Chung and R.G. Rajagopalan "CFD Analysis for Ducted Fans with Validation" AIAA 2003-4079, June 2003

[2] Leishman, Gordon J. "Principles of Helicopter Aerodynamics, 2nd edition" Cambridge University Press, New York, 2006

[3] Horn, Joseph F. and Eric Tobias "Flight Simulation of Advanced Ducted Fan Air Vehicles"

[4] Kruger, W. "On Wind Tunnel Tests and Computations Concerning the Problem of Shrouded Propellers" NACA TM 1202, 1949

[5] Mort, K.W. "Performance Characteristics of a 4-Foot-Diameter Ducted Fan at Zero Angle of Attack for Several Fan Blade Angles" NASA TN D-3122, 1965

[6] Mort, K.W. and B. Gamse "A Wind-Tunnel Investigation of a 7-Foot-Diameter Ducted Propeller" NASA TN D-4142, 1967

[7] Martin, Preston and Chee Tung "Performance and Flowfield Measurements on a 10-inch Ducted Rotor VTOL UAV" US Army Research, Development, and Engineering Command. Ames Research Center, Moffett Field, CA, 2004

[8] Ahn, Jon and Kyung Tae Lee "Performance Prediction and Design of a Ducted Fan System" AIAA 2004-4196, July 2004

[9] Lee, H.D., O.J. Kwon, and J. Joo "Aerodynamic Performance Analysis of a Helicopter Shrouded Tail Rotor Using an Unstructed Mesh Flow Solver" The 5th Asian Computational Fluid Dynamics, Busan, Korea, October 27~30, 2003

[10] Brinkman, H.C. "On the permeability of media consisting of closely packed porous particles" Applied Scientific Research, A1, 1947, pp.81-86

[11] Mital, Rajat and Gianluca Iaccarino "Immersed Boundary Methods" Annual Review Fluid Mechanics, 2005

[12] Cho, Yong, Jogesh Chopra and Philip J. Morris " Immersed Boundary Method for Compressible High-Reynolds Number Viscous Flow around Moving Bodies" AIAA 2007-125, 2007

[13] Peskin, C.S. "Flow patterns around heart valves: a numerical method' Journal of Computational Physics, 10, 1972, pp. 252-271

[14] Mohd-Yusof, J. "Combined immersed-boundary/B-Spline methods for simulations of flow in complex geometries" CTR Annual Research Briefs, NASA Ames Research/Stanford University, 1997, pp.317-327

[15] Menter, F.R. “Improved two-equation turbulence models for aerodynamic flows” NASA TM-103975, 1992

[16] Shu, C.W. “Essentially non-oscillatory and weighted essentially non-oscillatory schemes for hyperbolic conservation laws” ICASE Report No. 97-65, NASA/CR-97-206253, 1997

[17] Jameson, A., W. Schmidt, and E. Turkel “Numerical solution of the Euler equations by finite volume methods using Runge-Kutta time-stepping schemes” AIAA 81-1259, 1981

[18] Lockard, D.P. “Simulation of the Loading and Radiated Sound of Airfoils and Wings in Unsteady Flow Using Computational Aeroacoustics and Parallel Compurters” Ph.D. thesis, Pennsylvania State University, 1997

[19] Hixon, R. “Numerically Consistent Strong Conservation Grid Motion for Finite Difference Schemes” AIAA Journal, Vol. 38, No.9, September 2000

[20] Vanyo, James P. “Rotating Fluids in Engineering and Science” Stoneham, MA: Butterworth-Heinemann, 1993

[21] Liew, Yih-Pin “Computation of Interactions of Blast with Responding Solids using an “Embedded Solid” Approach” PhD Thesis, Pennsylvania State University, State College, PA, 2007

[22] Boelens, O.J, H. van der Ven, B. Oskam and A.A. Hassan “Accurate and efficient vortex-capturing for a helicopter rotor in hover” National Aerospace Laboratory NLR, Fluid Dynamics, August 2000

[23] Hariharan, Nathan and Lakshmi N. Sankar “A Review of Computational Techniques for Rotor Wake Modeling” AIAA-00-0114, 2000

[24] Hovey, R.W. “ Duct-Fan for Light Aircraft” Sixth Edition, February 1982

[25] Abbot, Iran H. and Albert E. von Doenhoff “Theory of Wing Sections” Dover publications, New York, 1959